This document is accepted manuscript for publication in Icarus.
Published version of this manuscript is found at https://doi.org/10.1016/j.icarus.2017.09.011

Initial Inflight Calibration for Hayabusa2 Optical Navigation Camera (ONC) for Science Observations of Asteroid Ryugu

H. Suzuki[1], M. Yamada[2], T. Kouyama[3], E. Tatsumi[4], S. Kameda[5], R. Honda[6], H. Sawada[7], N. Ogawa[7], T. Morota[8], C. Honda[9], N. Sakatani[1], M. Hayakawa[7], Y. Yokota[7], Y. Yamamoto[7], and S. Sugita[4]

[1]Meiji Univ. Kawasaki, Kanagawa

[2]Chiba Inst. Tech., Tsudanuma, Narashino, Chiba

[3]National Institute of Advanced Industrial Science and Technology, Tsukuba, Ibaraki

[4]Univ. of Tokyo, Hongo, Bunkyo, Tokyo

[5]Rikkyo Univ. Nishi-Ikebukuro, Toshima, Tokyo

[6]Kochi Univ., Kochi, Kochi

[7]Japan Aerospace Exploration Agency, Sagamihara, Kanagawa

[8]Nagoya Univ., Nagoya, Aichi

[9]Univ. of Aizu, Aizu Wakamatsu, Fukushima

Abstract.

Hayabusa2, the first sample return mission to a C-type asteroid was launched by the Japan Aerospace Exploration Agency (JAXA) on December 3, 2014 and will arrive at the asteroid in the middle of 2018 to collect samples from its surface, which may contain both hydrated minerals and organics. The optical navigation camera (ONC) system on board the Hayabusa2 consists of three individual framing CCD cameras, ONC-T for a telescopic nadir view, ONC-W1 for a wide-angle nadir view, and ONC-W2 for a wide-angle slant view will be used to observe the surface of Ryugu. The cameras will be used to measure the global asteroid shape, local morphologies, and visible spectroscopic properties. Thus, image data obtained by ONC will provide essential information to select landing (sampling) sites on the asteroid. This study reports the results of initial inflight calibration based on observations of Earth, Mars, Moon, and stars to verify and characterize the optical performance of the ONC, such as flat-field sensitivity, spectral sensitivity, point-spread function (PSF), distortion, and stray light of ONC-T, and distortion for ONC-W1 and W2. We found some potential problems that may influence our science observations. This includes changes in sensitivity of flat fields for all bands from those that were measured in the pre-flight calibration and existence of a stray light that arises under certain conditions of spacecraft attitude with respect to the sun. The countermeasures for these problems were evaluated by using data obtained during initial in-flight calibration. The results of our inflight calibration indicate that the error of spectroscopic measurements around 0.7 μm using 0.55, 0.70, and 0.86 μm bands of the ONC-T can be lower than 0.7 % after these countermeasures and pixel binning. This result suggests that our ONC-T would be able to detect typical strength (~3 %) of the serpentine absorption band often found on CM chondrites and low albedo asteroids with $\geq 4\sigma$ confidence.

Keywords Hayabusa2, Asteroid Ryugu, Instrumentation, Near-Earth objects

1. Introduction.

Hayabusa2 is a sample return mission to an asteroid 162173 Ryugu (provisional designation 1999 JU_3) by Japan Aerospace Exploration Agency (JAXA) (Tsuda et al., 2012, Tachibana et al., 2015). This is the first sample return mission to a C-type asteroid, which may contain both hydrated minerals and organics. The instruments on the Hayabusa2 spacecraft include the optical navigation camera (ONC) system that will observe the surface of Ryugu at the highest spatial resolutions. This camera system consists of three individual framing charge-coupled device (CCD) cameras, ONC-T for a telescopic nadir view, ONC-W1 for a wide-angle nadir view, and ONC-W2 for a wide-angle slant view (~30 degrees from the nadir). The cameras will be used to measure the global asteroid shape, local morphologies, and visible spectroscopic properties (Sugita et al., 2013a).

There is room for different interpretations for the visible spectroscopic observations of Ryugu. Although all the previous spectral observations supported that Ryugu is a C-complex asteroid, more subtle possible features, such as a positive UV slope and an absorption band at approximately 0.7 μm, which would influence the subclass of the asteroid in spectroscopic taxonomy, are not confirmed (Binzel et al., 1999; Vilas, 2008; Moskovitz et al., 2013; Lazarro et al., 2013; Sugita et al., 2013b; Perna et al., 2017). These discrepancies can reflect regional differences in appearance of spectra as asteroid rotates such that the spin axis is substantially tilted. However, such subtle spectral changes could be caused by issues of calibration of telescopic data. In either case, it is important for the ONC to observe the surface of Ryugu with high accuracy to properly characterize its spectral properties. The accurate characterization is essential for understanding the history of the asteroid as well as selecting good sampling sites for Hayabusa2, which will bring the first sample from a C-type asteroid to Earth in 2020 (Tsuda et al., 2012; Tachibana et al., 2015).

In order to achieve such spectroscopic characterization, a series of calibration experiments were conducted in laboratories prior to the launch and included the spectral response function, point spreading function (PSF), distortion, and stray light level. Many laboratory calibration results for ONC-T were discussed by Kameda et al. (2017), and meteorite measurement experiments with the ONC-T flight model were discussed by Kameda et al. (2015). Nevertheless, inflight calibrations are essential to warrant the quality of spacecraft data obtained during an actual mission because strong vibrations during launch and subsequent deployment in space could damage and change instruments. Hence, a proper and accurate analysis of inflight data is essential to ensure the quality of mission data reduction. Detailed descriptions of the afore-mentioned calibration data will also allow scientists to plan analyses of the data expected upon arrival at asteroid Ryugu and will also aid scientists in interpreting the data. Following the launch of Hayabusa2 on December 3, 2014, several images, such as that of deep space, stars, Earth, Moon, Mars, and ONC-T onboard lamps were captured using the three cameras.

The purpose of this study involves deriving calibration data necessary for data reduction, estimating errors for calibrated data based on analyses of inflight image data, and comparing the calibrated data with pre-flight data. The rest of the paper is organized as follows. The design of W1 and W2 is discussed in section 2. Their distortion is discussed in section 3. Their spectral sensitivities are discussed in sections 4. The PSF of ONC-T is examined in section 5, its distortion is investigated in section 6, its spectral sensitivity is studied in section 7, and stray light is discussed in section 8. The implications of the results of our calibrations for the upcoming observations of Ryugu are discussed in section 9 before conclusion in section 10.

2. Design of ONC W1 and W2

ONC-W1 and W2 are wide view (> 65 deg × 65 deg) panchromatic cameras mainly used for optical navigation during cruise and low-altitude operations near the asteroid. The design of the two cameras is almost identical except for the transmittance of the ND filter and the viewing direction relative to the spacecraft. The field of view of W1 was aligned in the −Z direction in the spacecraft coordinate system (i.e., nadir viewing), while that of W2 was slanted by approximately 30 degrees from the −Z direction. The positions of W1 and W2 in the spacecraft are illustrated in Fig 1 in Kameda et al., 2017 (hereafter referred to as K2017). The definition of image coordinates and its relationship with the spacecraft coordinate system for three cameras are summarized in Figure 1. Additionally, W1 and W2 are expected to obtain detailed pictures of the surface of Ryugu during touch down procedures. The major specifications of W1 and W2 are summarized in Table 1. The specifications of ONC-T are listed in K2017 in the same manner. The radiometric response (sensitivity) of the cameras depends on the transmittances of fore optics ($T_{opt}(\lambda)$) and ND filters ($T_{ND}(\lambda)$), the quantum efficiency ($Q(\lambda)$) of CCD, and the F-number. Measured transmittances and $Q(\lambda)$ provided by the CCD manufacturer (E2V) are shown in Figures 2. The verification of sensitivity of W1 and W2 cameras was performed by using images of Earth captured during the swing-by phase of cruising. Details of the verification are described in section 4.

Table 1. Specification of ONC-W1 and W2.

	ONC-W1 and W2
F number (F#)	9.6
Effective aperture diameter	1.08 mm
Focal length (Measured)	W1 : 10.22 mm W2 : 10.38 mm
Field of view (FOV) (Measured)	W1: 69.71 deg (Nadir view) W2 : 68.89 deg (Slanted ~30 degrees from nadir)
CCD format	1024(H) pixels ×1024(V)pixels E2V CCD47-20 (AIMO)
CCD pixel size	13 µm × 13 µm
Mean pixel resolution (Measured)	W1: 0.06808 degrees/pixel W2: 0.06728 degrees/pixel
Transmittance of ND filter	W1: 7%, W2: 20% (see Figure 1)
Sensitivity flatness (Measured)	W1: 67.3% and 72.0% at corners of the FOV.* W2: 82.8% and 82.9% at corners of the FOV. * (*Values normalized by sensitivity at center of the FOV.)
Pixel sampling rate	3 MHz
A/D conversion	12-bit
Gain factor	20.95 e^-/DN

Exposure time	W1: 0 s, 170 μs, 256 μs, 340 μs, 513 μs, 680 μs, 1.03 ms, 1.36 ms, 2.05 ms, 2.72 ms, 4.10 ms, 5.44 ms, 8.20 ms, 10.9 ms, 16.4 ms, 21.8 ms, 32.8 ms, 43.5 ms, 65.6 ms, 87.0 ms, 131 ms, 174 ms, 262 ms, 348 ms, 525 ms, 696 ms, 1.05 s, 1.39 s, 2.10 s, 2.79 s, 4.20 s, 5.57s W2: 0 s, 1.36 ms, 2.05 ms, 2.72 ms, 4.10 ms, 5.44 ms, 8.20 ms, 10.9 ms, 16.4 ms, 21.8 ms, 32.8 ms, 43.5 ms, 65.6 ms, 87.0 ms, 131 ms, 174 ms, 262 ms, 348 ms, 525 ms, 696 ms, 1.05 s, 1.39 s, 2.10 s, 2.79 s, 4.20 s, 5.57 s, 8.40 s, 11.1 s, 16.8 s, 22.3s, 33.6s, 44.6s

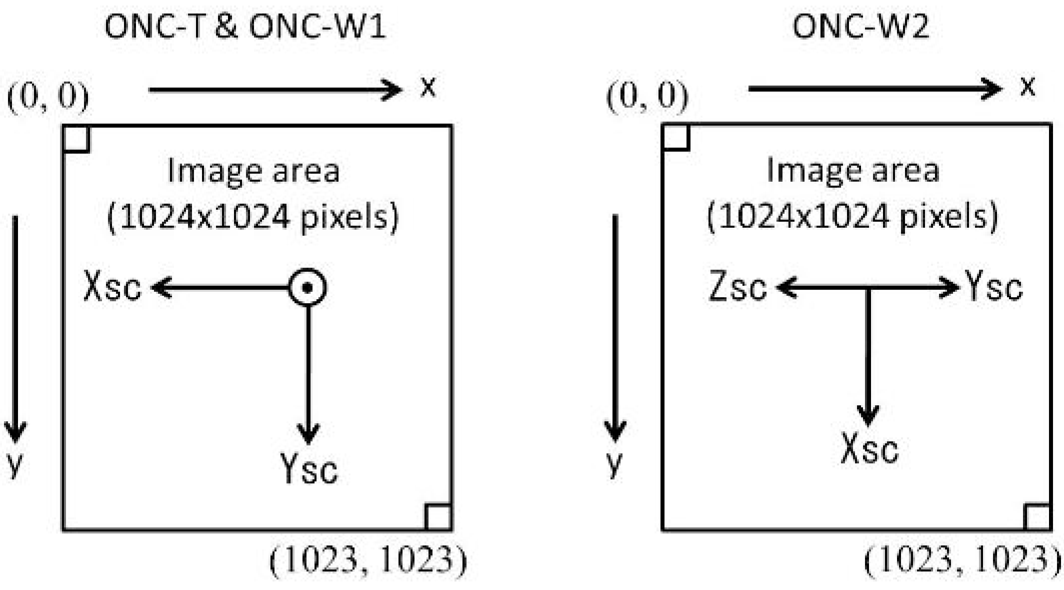

Figure 1. Definition of image coordinate system for (left) ONC-T, ONC-W1 and (right) ONC-W2. Xsc, Ysc, and Zsc indicate the spacecraft coordinate system (For definition, see Figure 22a). Since the center of FOV is slanted from nadir direction, none of the spacecraft axes (Xsc, Ysc, and Zsc) are normal to CCD of ONC-W2.

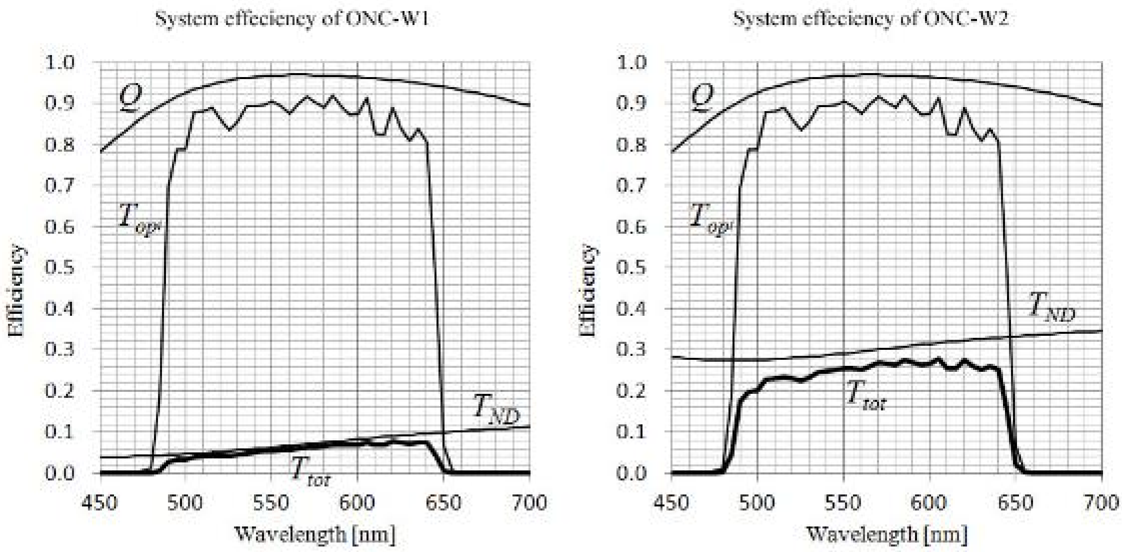

Figure 2. System efficiencies of ONC-W1 (left) and W2 (right). Quantum efficiency, Q (number of photoelectrons per single photon), the transmittance T_{opt} of the optical system, the transmittance T_{ND} of neutral density filter, and the total transmittance *Ttot* of the entire camera system are shown in the Figure.

3. Distortion of ONC-W1 and -W2

As noted above, W1 and W2 cameras have a wide field of view (FOV > 65 degrees), and thus distortion in the peripheral areas in their FOV is not negligible. The degree of distortion was measured in pre-flight calibration experiments by using a flat liquid crystal display (LCD) and an image with equally spaced dot patterns. Figure 3 (a) shows an image of the dot pattern displayed by the large LCD (50 inches). This image was taken by the W1 camera facing the LCD at a distance of 475 mm. It is noted here that because ONC-W1 and W2 cameras have large depth of field (F number = 9.6), even an image on LCD at small distance (50 cm) from cameras do not require a collimator for the measurements. As the distance from an image center increases, spaces between the neighboring dots in the image captured by the CCD decrease due to the distortion of the optics. An ideal optics with infinitesimal aperture size (e.g., a pinhole system) without a distortion should project the dot pattern with constant spaces on an image sensor (CCD). In such a system, an image of a point light source located at α radians from the center of FOV is projected on the image sensor at distance r' [pixels] measured from its center:

$$r' = \frac{f}{p}\tan\alpha \quad \text{[pixels]}$$

where f denotes a focal length of a camera, and p denotes the size of CCD pixels. However, in real optics, the point source is projected at a distance r [pixels] from the center of the image due to the distortion. The distortion parameters (ϵ_1 and ϵ_2) are defined by the relationship between r' and r as follows:

$$r' = r + \epsilon_1 r^3 + \epsilon_2 r^5. \quad (1)$$

The model was used to define the distortion of W1 and W2 cameras in the pre-flight calibration. The estimated parameters are listed in Table 2. An image of the dot patterns corrected by using these parameters is shown in Figure 3 (b). The barrel-shaped distortion shown in the original image (Fig 3(a)) is corrected in Figure 3 (b).

However, the camera distortion parameters after launch may have changed from the pre-flight values due to severe vibration during the launch and large changes in environmental conditions, such as temperature. Thus, these distortion parameters were examined by using post-launch star images captured on Feb 19, 2015 (W1) and Dec 11, 2014 (W2). A left (Right) panel in Figure 4 shows the positions of stars identified in the inflight image captured by the W1 and W2 cameras. The positions of stars are defined as locations in which maximum signal from each star is detected. The circle symbols in each panel show the original positions of the identified stars in an image coordinate system. Exposure times for these acquisitions corresponded to 5.57 s and 44.57 s for the W1 and W2 cameras, respectively. Original star positions in the image coordinate system were manually determined by using an astronomical imaging and data visualization application (SAOimage DS9) distributed by Smithsonian Astrophysical Observatory. These positions were then converted to distortion-free positions by using the coefficients listed in Table 2 and Equation (1). A result of this conversion is demonstrated by plus symbols in each panel of Figure 4. The new positions of the stars were considered as results of a projection in the pinhole system, and the actual angles between the image center and each star were accurately estimated by providing the f and p values. These angle values were used to project each star on an arbitral spherical coordinate system. A set of Euler angles (α, β, γ) was then calculated to convert the spherical coordinates to the celestial coordinates. Finally, corresponding right ascension and declination angles were obtained for each pixel. Figure 5 shows the results of this procedure to determine the celestial coordinates for the star images captured by the (a) W1 and (b) W2 cameras. The FOV in x-direction, y-direction, and diagonal direction were estimated as 69.71 (68.89) degrees and 91.58 (90.75) degrees for W1 (W2). The mean pixel resolutions were estimated as 0.06808 [degrees/pixel] and 0.06728 [degrees/pixel] for W1 and W2, respectively. An error between the estimated celestial coordinate values and known R.A and Dec angles for each star (in J2000 system) corresponded to averages of 0.041 degrees and 0.036 degrees for W1 and W2, respectively. Thus, random errors in the estimation of the celestial coordinate of the star images captured inflight calibration are listed in Table 2 and are less than the pixel resolutions. This shows that the distortion parameters measured in the pre-flight calibration (see Table 2) did not deteriorate after the launch.

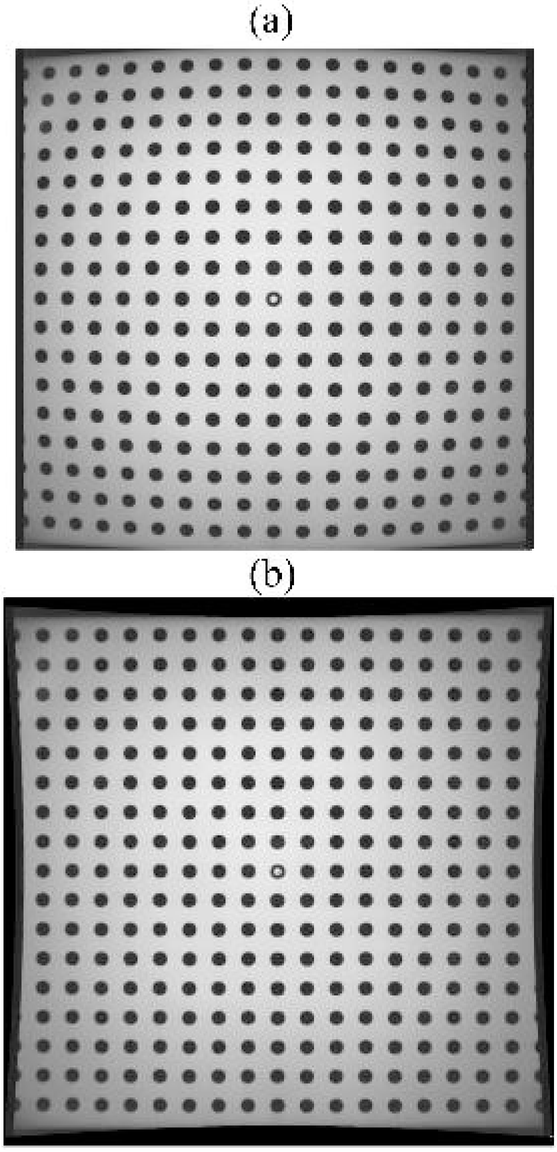

Figure 3. (a) An image of the dot pattern displayed by the large LCD (W1 image). (b) Distortion-corrected image obtained by using the parameters listed in Table 2.

Table 2. Distortion parameters of W1 and W2 cameras determined in the pre-flight calibration experiment.

	W1	W2
ϵ_1 [pixel^{-2}]	3.134E-7	2.893E-7
ϵ_2 [pixel^{-4}]	-1.716E-13	-1.365E-13
RMS Error [pixels] (after correction)	0.6	0.5

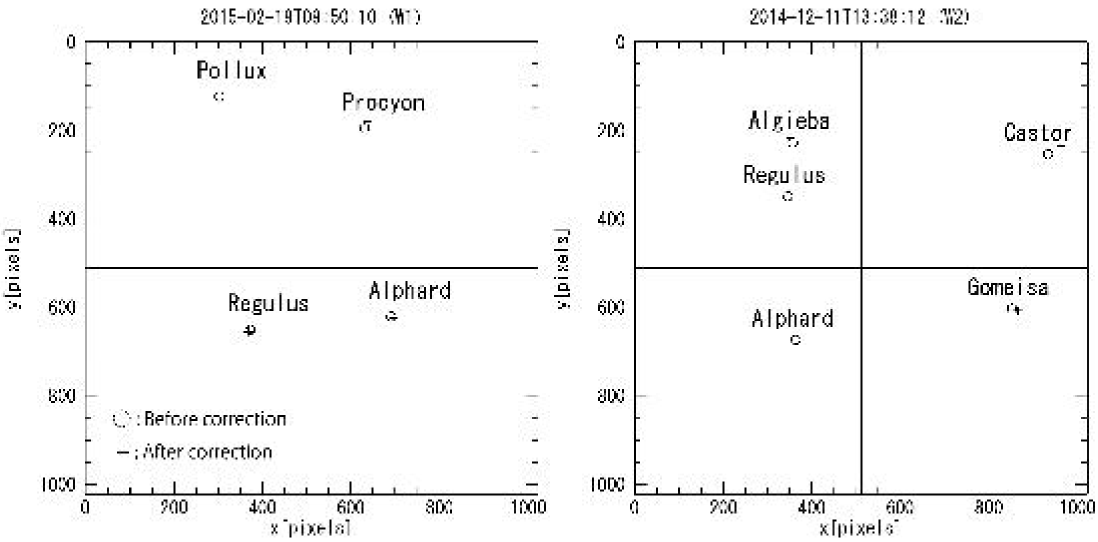

Figure 4. The positions of stars identified in the inflight image captured by W1 (left) and W2 (right) cameras. Open circle symbols in each panel show the original positions of identified stars in an image coordinate system. Plus symbols show the distortion-corrected position of the stars.

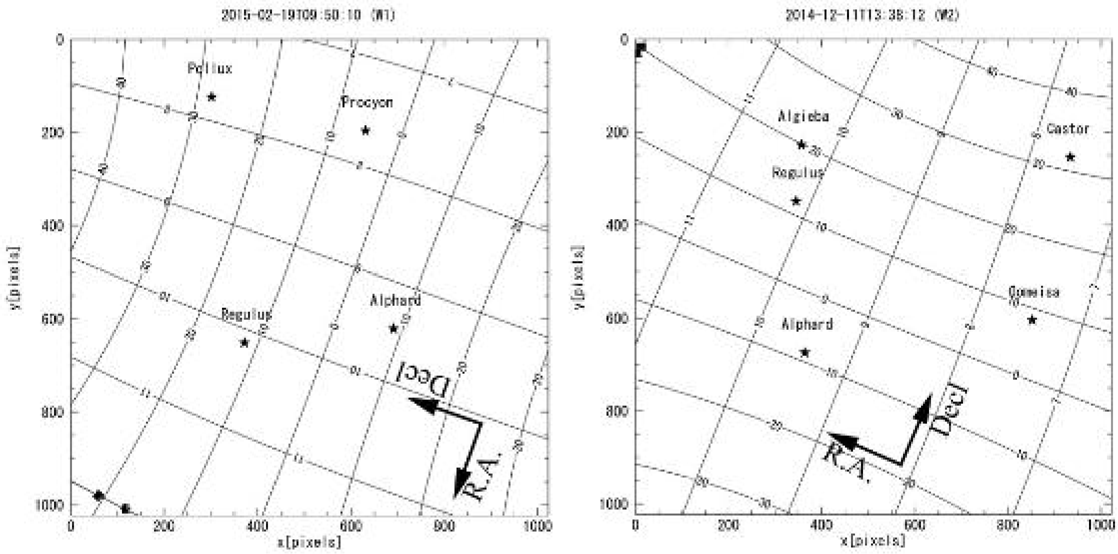

Figure 5. The results of fitting of R.A and Decl angles to the original images observed by W1 (left) and W2 (right) cameras.

4. Verification of Sensitivity of ONC-W1 and -W2

Images of the Earth were acquired immediately before and after the swing-by phase by both wide cameras to check the functioning of the cameras. Observations of the Earth by W2 were performed immediately prior to the swing-by on Dec 3, 2015. Table 3 lists the times, exposure settings, and distances to the Earth for the observations. Twenty successive images were obtained by W2 during the approaching phase of a swing-by. A composite image composed using images #1, #7, #13, #17 and #19 are shown in Figure 6 with a common gray scale. Images of approaching Earth and smear patterns (vertical stripes) were observed. This is kind of frame transfer smear. The reason why the smear presents both above and below bright object (the Earth) is due to a mechanism of resetting and transferring charges before and after the exposure. Because no zero-exposure images were taken for smear correction, smear counts were estimated based a dark area in each image and subtracted from the raw images. The dark area defined in this calculation includes a region above the dashed line (y = 455 pixels) as shown in Figure 6. The smear counts in each row of images were estimated by averaging the counts in the dark area along the y-axis. The obtained signal levels were compared with an expected value defined as follows. A solar irradiance illuminating unit area of the Earth's surface with a zenith angle of χ at a wavelength λ is defined as $J_s(\lambda)\cos\chi$ [W/m^2 nm]. The radiance of reflected light from the Earth's surface with a bidirectional reflectance factor of $R(\lambda, \chi, \theta, \emptyset)$ is expressed as follows:

$$I(\lambda, \chi, \theta, \emptyset) = \frac{R(\lambda,\chi,\theta,\emptyset)\, J_s(\lambda)\cos\chi}{\pi} \ [\mathrm{W/m^2\ nm\ sr}] \qquad (2)$$

where, θ and $\emptyset$ denote spacecraft zenith angle, and azimuth angle measured from the sun direction [Martonchik et al., 2000]. The number of photons entering a single pixel of the camera facing the plane with the radiance $I(\lambda, \chi, \theta, \emptyset)$ is as follows:

$$N(\lambda, \chi, \theta, \emptyset) = \frac{I(\lambda,\chi,\theta,\emptyset)}{h\nu} T_{opt}(\lambda)\, T_{ND}(\lambda) A\Omega = \frac{I(\lambda,\chi,\theta,\emptyset)}{h\nu} T_{opt}(\lambda)\, T_{ND}(\lambda) \left(\frac{\pi D^2}{4}\right)\left(\frac{p^2}{f^2}\right) \ [\mathrm{Photons/s\ nm}] \quad (3)$$

where h is Plank constant, ν is frequency of a photon, A and Ω denote the area of effective aperture and the solid angle of a pixel ($\Omega = p^2/f^2$), respectively. $T_{opt}(\lambda)$ and $T_{ND}(\lambda)$ denote optical transmittances of the optics and an ND filter, respectively as shown in Figure 2. Additionally, p, f and D denote the pixel size (=13 μm), the focal length of a camera (see Table 1), and the diameter of the effective aperture of optics, respectively. Thus, by using equations (2) and (3), the total signal obtained with an exposure time τ is expressed as follows:

$$S = \frac{\tau}{G}\int_{450\mathrm{nm}}^{700\mathrm{nm}} N(\lambda, \chi, \theta, \emptyset) Q(\lambda)\mathrm{d}\lambda = \frac{\bar{R}(\chi,\theta,\emptyset)\tau\cos\chi}{4hc\,G}\left(\frac{p^2}{F^2}\right)\int_{450\mathrm{nm}}^{700\mathrm{nm}} \lambda J_s(\lambda) T_{opt}(\lambda)\, T_{ND}(\lambda) Q(\lambda)\mathrm{d}\lambda \ [\mathrm{DN}], (4)$$

where F denotes an F-number defined by $F \equiv \frac{f}{D}$ and G denotes the gain factor of CCD (see Table 1). In this transformation, R is assumed to be nearly constant throughout the bandpass of the cameras (450-700nm) and taken it out of the integral. This "mean bidirectional reflectance factor" is denoted as $\bar{R}$ in the equation. Obviously, this simplification is not strictly valid for all terrain surfaces as Earth has colorful appearance in the visible wavelength range. Nevertheless, this equation is useful for estimating an which order of magnitude the signal level may have in digital number unit (DN) when the camera acquired an image of a plane with the mean bidirectional reflectance factor, $\bar{R}(\chi, \theta, \emptyset)$, and the solar irradiance $J_s(\lambda)$. Figure 7 shows a map of the $\bar{R}(\chi, \theta, \emptyset)$ calculated from image #17 (see Table 3 and Fig. 6) by using equation (4). Validation of the observation is conducted by comparing the reflectance factor of the ocean with a reference value. Nearly middle point in Arabian Sea (shown with plus symbol in Figure 7) is focused on for this comparison since there are no overlaying clouds. Geographic location, observed mean bidirectional reflectance factor, and geometric parameters$(\chi, \theta, \emptyset)$ for this region are listed in Table 4 together with reference values. The reference values are estimated by converting satellite-based 'anisotropic reflectance factors' reported in Taylor and Stowe, [1984] to $\bar{R}(\chi, \theta, \emptyset)$. Geometric parameters $(\chi, \theta, \emptyset)$ for the reference value correspond to 37-40 degrees, 48 degrees, and 167 degrees, respectively and nearly identical with present case. The $\bar{R}$ value of sea surface observed by ONC-W2 is found to be 40% less than the reference value. They agree within a half order of magnitude.

A similar evaluation was also performed for the images obtained by the W1 camera. Observations of the Earth by W1 were performed after the swing-by on Dec 4, 2015. Table 4 lists the times, exposure settings, and distances to the Earth at the observations. Figure 8 shows a trimmed image of the Earth captured by the W1 camera with a gray scale (#1 of Table 7). A map of $\bar{R}(\chi, \theta, \emptyset)$ evaluated from this image and equation (4) is shown in Figure 9. An area with high value up to 0.8 corresponds to the Antarctic continent. Such high reflectance value is due to the surface covered with snow and ice and is well consistent with results from satellite observations [Taylor and Stowe, 1984; Hatzianastassiou et al., 2014]. Two distinct areas are selected for the comparison between the observed values and the reference values by Taylor and Stowe, [1984]. The one is on Antarctic continent and the other is on Antarctic Sea as indicated with plus symbols in Figure 9. Geographic locations, observed mean bidirectional reflectance factors, and geometric parameters $(\chi, \theta, \emptyset)$ for these regions are listed in Table 6 together with the reference value. In this case, the $\bar{R}$ value of sea surface (Antarctic Sea) observed by ONC-W1 is found to be 70% greater than the reference value. They agree within an order of magnitude. On the other hand, the observed $\bar{R}$ value for the snow surface (Antarctic continent) shows fairly good agreement with the reference value. In addition, $\bar{R}$ values for ocean and cloud areas shows comparable value with results from W2 observations. Thus, signal levels for Earth consistent with expectation from equation (4) were obtained by both W1 and W2 cameras suggesting no severe degradation in sensitivity for these cameras after the launch.

Table 3. Times, exposure settings, and distances to the Earth for the observations by the W2 camera.

Data# (Filename)	Observation time YYYY-MM-DDTHH:mm:SS	Exposure time [sec]	Distance to the Earth [km]
#1(hyb2_onc_20151203_000006_w2f_l2a)	2015-12-03T00:00:06	0.0041	202863.4
#2(hyb2_onc_20151203_005958_w2f_l2a)	2015-12-03T00:59:58	0.0041	184855.2
#3(hyb2_onc_20151203_015958_w2f_l2a)	2015-12-03T01:59:58	0.0041	166674.6
#4(hyb2_onc_20151203_025958_w2f_l2a)	2015-12-03T02:59:58	0.0041	148333.6
#5(hyb2_onc_20151203_035958_w2f_l2a)	2015-12-03T03:59:58	0.0041	129793.9
#6(hyb2_onc_20151203_045958_w2f_l2a)	2015-12-03T04:59:58	0.00272	111001.3
#7(hyb2_onc_20151203_052958_w2f_l2a)	2015-12-03T05:29:58	0.00272	101486.5
#8(hyb2_onc_20151203_055958_w2f_l2a)	2015-12-03T05:59:58	0.00272	91875.2
#9(hyb2_onc_20151203_062958_w2f_l2a)	2015-12-03T06:29:58	0.00272	82150.0

#10(hyb2_onc_20151203_065958_w2f_l2a)	2015-12-03T06:59:58	0.00272	72288.1
#11(hyb2_onc_20151203_071458_w2f_l2a)	2015-12-03T07:14:58	0.00272	67296.8
#12(hyb2_onc_20151203_072958_w2f_l2a)	2015-12-03T07:29:58	0.00272	62259.2
#13(hyb2_onc_20151203_074458_w2f_l2a)	2015-12-03T07:44:58	0.00272	57170.0
#14(hyb2_onc_20151203_075958_w2f_l2a)	2015-12-03T07:59:58	0.00272	52023.0
#15(hyb2_onc_20151203_081458_w2f_l2a)	2015-12-03T08:14:58	0.00272	46810.9
#16(hyb2_onc_20151203_082958_w2f_l2a)	2015-12-03T08:29:58	0.00272	41526.2
#17(hyb2_onc_20151203_084458_w2f_l2a)	2015-12-03T08:44:58	0.00272	36161.4
#18(hyb2_onc_20151203_085958_w2f_l2a)	2015-12-03T08:59:58	0.00272	30712.5
#19(hyb2_onc_20151203_091458_w2f_l2a)	2015-12-03T09:14:58	0.00272	25188.8
#20(hyb2_onc_20151203_092958_w2f_l2a)	2015-12-03T09:29:58	0.00272	19647.2

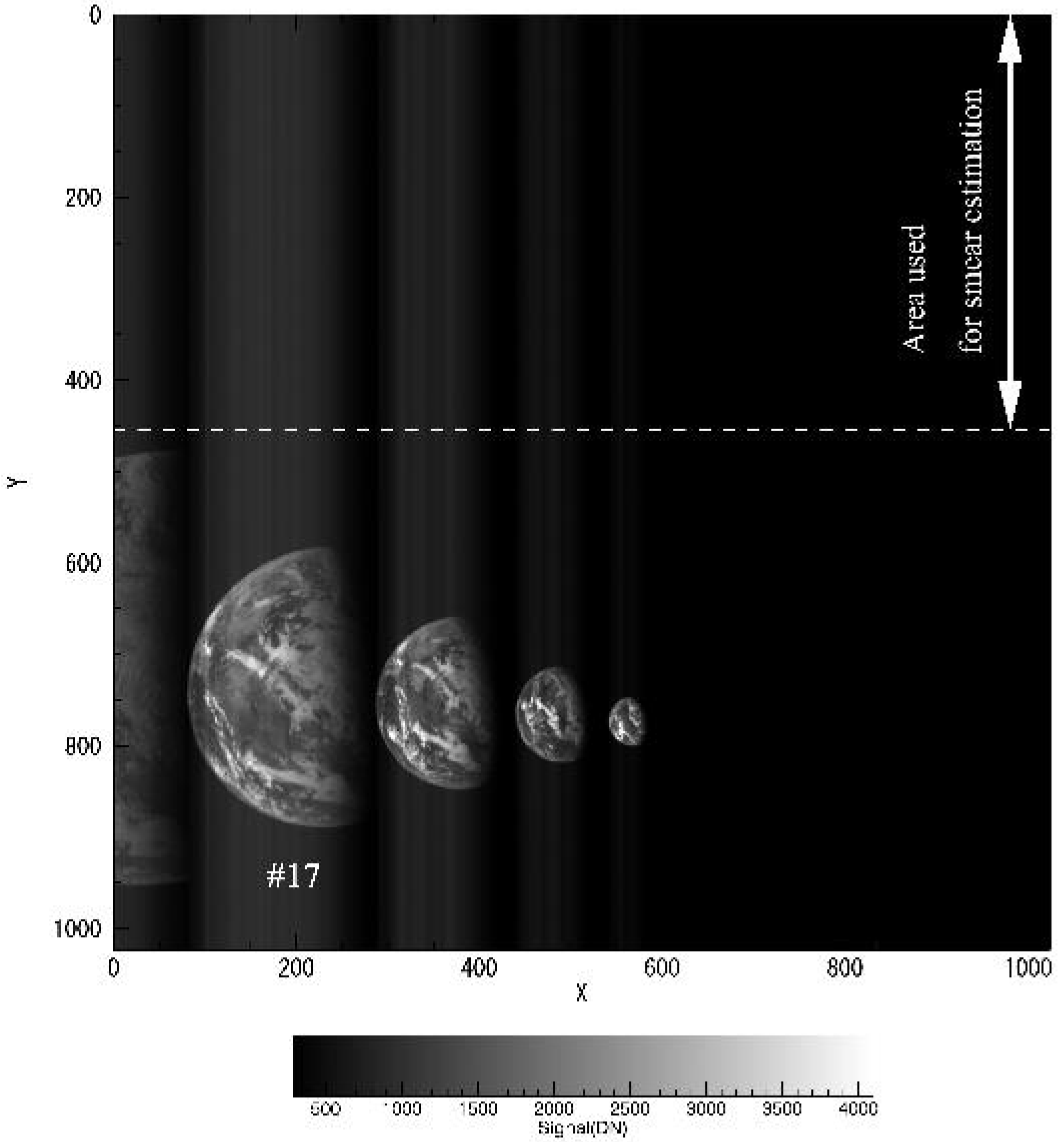

Figure 6. An image composed using images #1, #7, #13, #17 and #19. The top of the Earth image covers Sahara desert and the Mediterranean Sea, and the middle to lower left of the image covers Arabian Peninsula to Indian subcontinent.

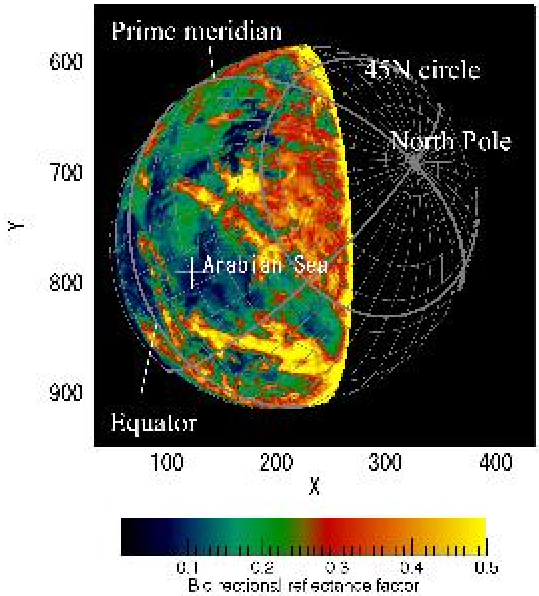

Figure 7. Bidirectional reflectance factor calculated from the image (#17 of Table 3) captured by the W2 camera.

Table 4. The observed and the reference value of R and geometric parameters (ONC-W2).

Area (location)	Surface type	Observed $\bar{R}(\chi,\theta,\emptyset)$	χ [deg]	θ [deg]	$\emptyset$ [deg]	$\bar{R}$ estimated from Taylor and Stowe [1984]
Arabian Sea (66.2E, 20.4N)	water	0.08	46.8	39.7	153.9	0.13

Table 5. Times, exposure settings, and distances to the Earth for the observations captured by the W1 camera.

Data# (Filename)	Observation time	Exposure time [sec]	Distance to the Earth [km]
#1(hyb2_onc_20151204_041027_w1f_l2a)	2015-12-04T04:10:27	0.082	342622.8
#2(hyb2_onc_20151204_045429_w1f_l2a)	2015-12-04T04:54:29	0.082	355423.0

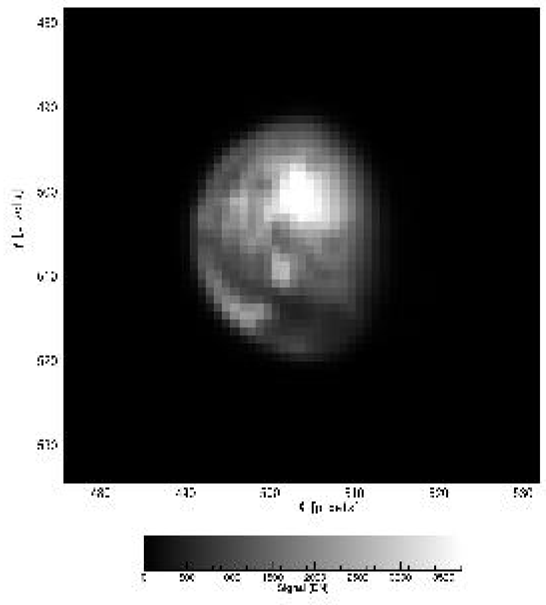

Figure 8. Trimmed image of the Earth captured by the W1 camera (#1 of Table 5). The brightest region is Antarctic continent.

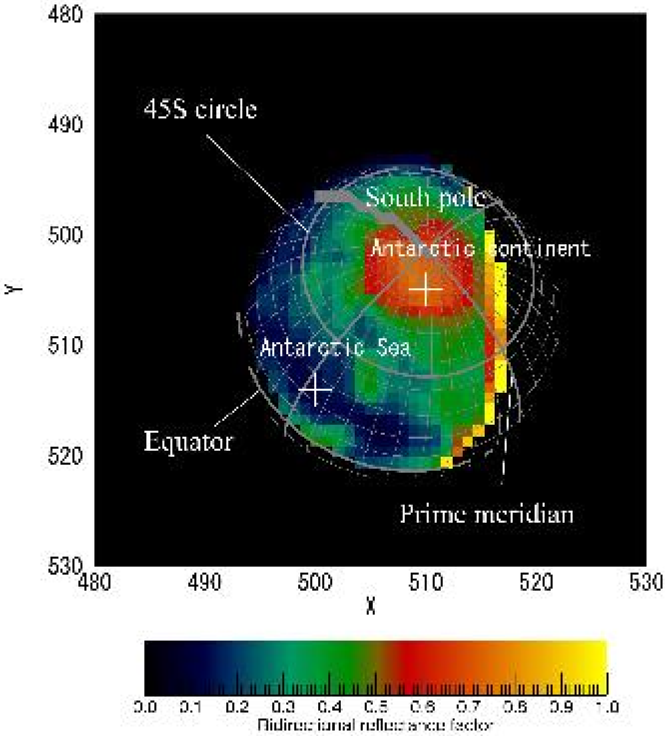

Figure 9. Bidirectional reflectance factor calculated from the image (#1 of Table 4) captured by the W1 camera.

Table 6. The observed and the reference value of R and geometric parameters (ONC-W1).

Area (location)	Surface type	Observed $\bar{R}(\chi, \theta, \emptyset)$	χ [deg]	θ [deg]	$\emptyset$ [deg]	$\bar{R}$ estimated from Taylor and Stowe [1984]
Antarctic continent (45.3E, 75.3S)	snow	0.72	63.5	15.1	46.2	0.73
Antarctic Sea (86.1E, 24.7S)	water	0.17	26.6	40.8	107.0	0.10

5. Verification of PSF of ONC-T using star images

In this section, the result of a measurement of the point-spreading function (PSF) of ONC-T using star images obtained during the initial check-out immediately after the launch is presented in comparison with the pre-launch PSF values measured with a star simulator comprising a collimator and a pinhole in a laboratory (K2017). A pre-flight image captured on Dec 11, 2014 with the wide-band filter (see K2017 for details) was used to estimate PSF. The exposure time to capture this image was set as 11.14 s. The left panel in Figure 10 shows an expanded image with a reference gray scale level. Twenty two stars were identified from this image, and each of the stars was assigned an identification number (from #1 to # 22). The right panel of Figure 10 shows the location and number of each star. The Hipparcos catalogue numbers (HIP ID) and visual magnitudes of these stars are listed in Table 7 in conjunction with the approx. pixel locations in the image. A two-dimensional Gaussian fitting method was applied to estimate the FWHM of each star image. The fitting was performed with an IDL function (GAUSS2DFIT). This function fitted a two-dimensional elliptical Gaussian equation to each star image and estimated the peak intensity, location, standard deviations along elliptical major and minor axes (σ_1 and σ_2), and the intensity of background. Additionally, σ_1 was adopted as an estimated standard deviation. σ_1 was then converted to FWHM by FWHM=2.35× σ_1. The estimated FWHM is shown in Figure 11 as a function of the distance from center of the image. The values obtained in the pre-flight (laboratory) calibration from K2017 are also shown in the plot for comparison. This result from the inflight calibration shows that the PSF of ONC-T (wide band) was less than 2 pixels in most fields of view (r < 575 pixels), indicating no evidence for degradations of PSF after the launch. The PSF outside this area was slightly higher than 2 pixels, and this was due to the vignetting by the extended hood attached to the camera after the pre-flight calibration to eliminate strong stray light coming through the fore optics system as discussed by K2017.

Table 7. The Hipparcos catalogue numbers (HIP ID) and visual magnitudes of stars identified in an image captured on Dec 11, 2014.

Star #	Hipparcos Cat #	Vis magnitude	x [pixels]	y [pixels]
1	HIP 24129	8.37	491	456
2	HIP 23946	8.34	435	531
3	HIP 23883	5.84	465	568
4	HIP 23909	8.53	483	558
5	HIP 23784	7.13	590	628
6	HIP 24063	7.52	543	490
7	HIP 24163	8.09	585	453
8	HIP 24158	8.07	545	450
9	HIP 24822	4.96	576	151
10	HIP 24761	7.30	525	173
11	HIP 24512	6.26	590	298
12	HIP 24820	6.12	261	113
13	HIP 24977	6.20	216	41
14	HIP 24906	6.65	176	61
15	HIP 23871	5.28	258	551
16	HIP 23949	6.51	171	501
17	HIP 23068	5.79	791	981
18	HIP 23088	5.79	971	985
19	HIP 23900	5.50	877	604
20	HIP 23550	7.44	976	773

21	HIP 24665	6.85	876	255
22	HIP 23151	7.99	883	950

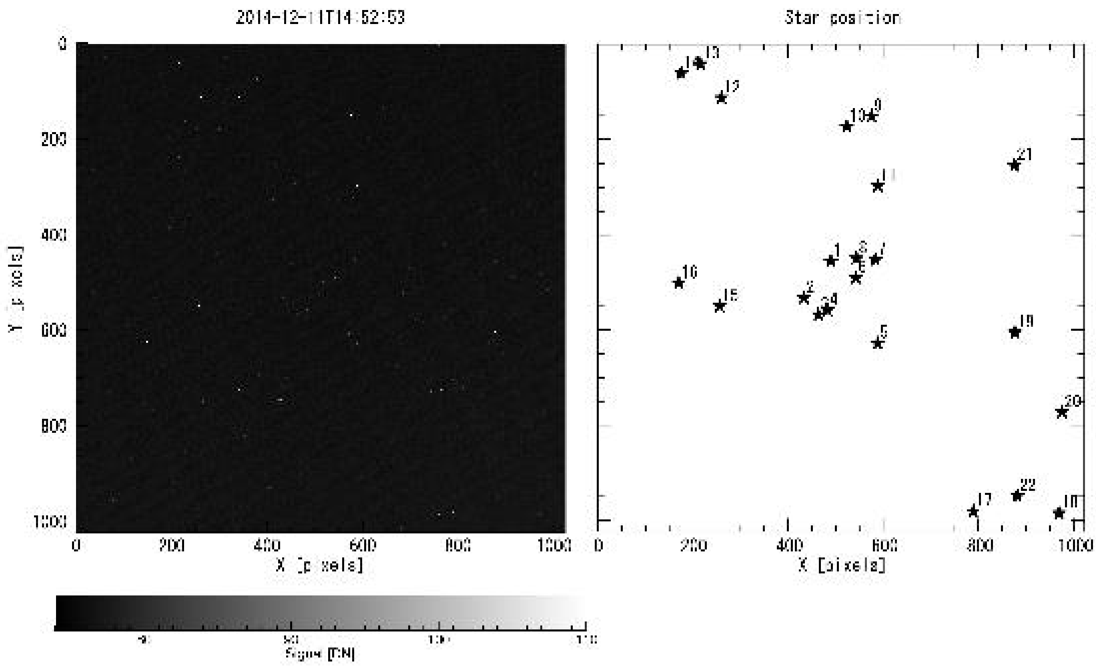

Figure 10. Star image captures with ONC-T on Dec 11, 2014 with the wide-band filter used in measurements of PSF and a distortion. A left panel shows an image with a reference gray scale level. A right panel shows the location and number of known stars.

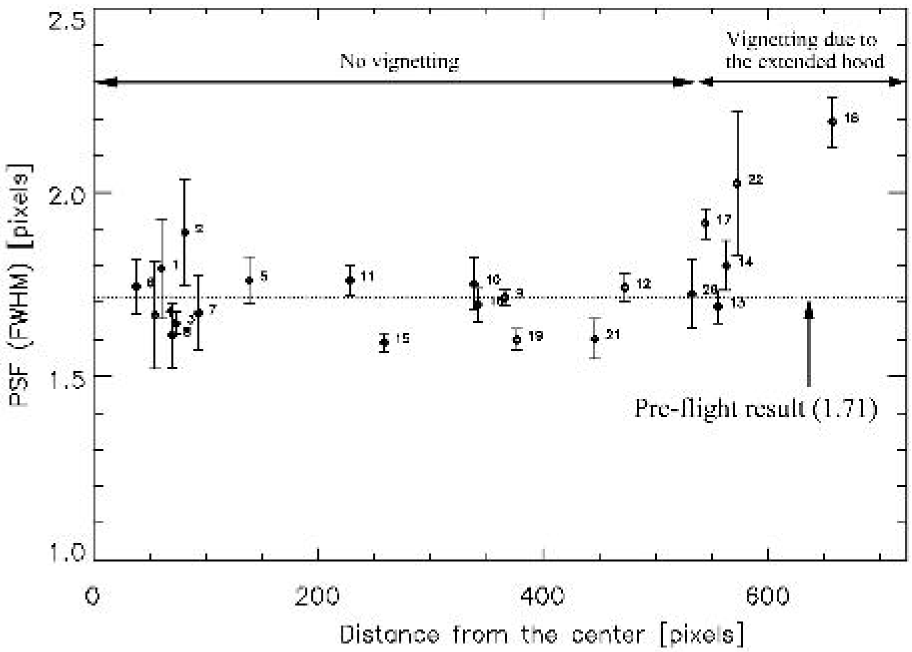

Figure 11. The estimated FWHM as a function of the distance from the center of the image. Note that the pre-flight measurements were conducted without a hood.

6. Estimation of a distortion and focal length of ONC-T using star images

The ONC-T is a telescopic camera with a narrow field of view corresponding to approximately 6.3 degrees[2]. Thus, in contrast to the W1 and W2 cameras, a distortion over the field of view was small. Thus, it was difficult to precisely determine the distortion of ONC-T in the same manner in the pre-flight calibration for W1 and W2; no distortion value was estimated for ONC-T before the launch. A star field taken from space offered much better data to estimate the distortion of the optics. The image of a star field used for the PSF verification (see Section 5) was also employed for an estimation of a distortion and the focal length of ONC-T. A model of the distortion is defined in an almost similar manner for the case of W1 and W2 cameras (see Section 3) as follows:

$$r' = r + \epsilon_1 r^3 \ \text{[pixels]}, \qquad (5)$$

where ϵ_1 denotes a distortion coefficient that yields *pincushion distortion* or *barrel distortion* depending on whether it is positive or negative [Owen, 2011]. Additionally, r' and r denote distances from the center of the image in an image coordinate system without and with a distortion, respectively. Furthermore, r' of 22 stars listed in Table 7 can be obtained by assuming coordinates (R.A and Decl.) corresponding to the center of the image (RA_c, DEC_c) and a focal length f_T of ONC-T by using equation (5). Moreover, r denotes the measured values obtained by $r = \sqrt{x^2 + y^2}$ for the identified 22 stars listed in Table 7. The best values of ϵ_1, (RA_c, DEC_c), and f_T for this model were estimated by an iteration as $-9.28 \times 10^{-9}[pixel^{-1}]$, (5.159 h, 21.961 deg), and 120.50±0.01 mm, respectively. Figure 12 shows the celestial coordinates fitted to the star images by assuming these parameters. The method of the fitting is described in section 3. This result shows that the magnitude of the distortion term in equation (5) ($\epsilon_1 r^3$) are nearly 1 pixel and 3 pixels at *r*=500 (the edge of an inscribed circle of FOV) pixels and *r*=724 pixels (the four corners of the FOV), respectively. The FOV in the x-direction, y-direction, and diagonal direction were estimated as 6.302 degrees and 8.881 degrees, respectively. The mean pixel resolutions were estimated as 0.0062 [degrees/pixel]. The standard error between the estimated celestial coordinate values and the known R.A and Dec angles for each star (in J2000 system) corresponds to 0.006 degrees. Thus, the accuracy of the distortion correction is about 1/10 pixel, which is sufficiently low to be negligible for the co-registration between different bands for visible spectroscopic observations. The higher accuracy is of great importance because it will be used for observing the global multi-band images of Ryugu (Sugita et al., 2013a).

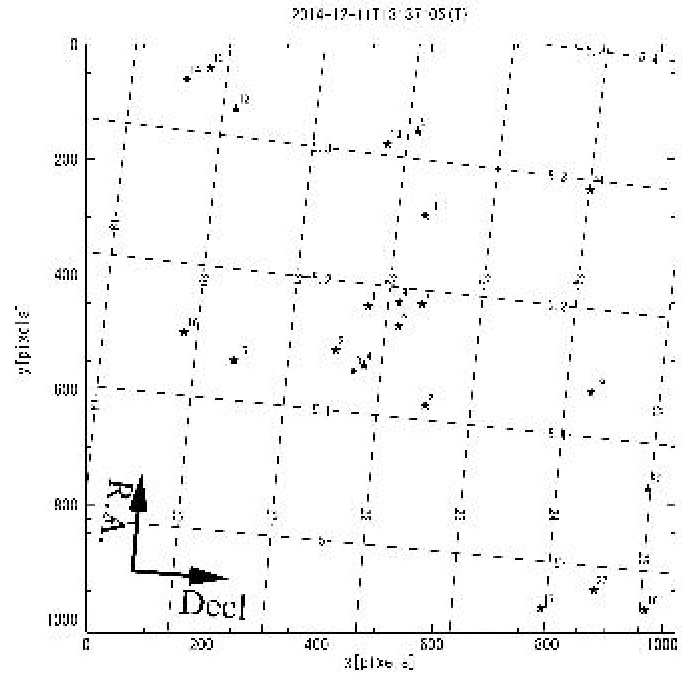

Figure 12. Celestial coordinates fitted to the star image by ONC-T.

7. Verification of Spectral Sensitivity and a flat field of ONC-T

In this section, the results of verification of spectral sensitivity and a flat field of ONC-T through the inflight observation of Mars, Moon, and the Earth are reported. In section 7-1, verification for relative sensitivity among all bands except for wide-band of ONC-T is conducted by comparing spectral reflectance measured with a ground-based observation and that deduced from multiband images by ONC-T. In section 7-2, radiometric calibrations by using a lunar spectral model (SELENE/SP model) are conducted. In particular, an uncertainty in the flatness of sensitivity among the three filter bands used for the searching for possible 0.7 μm absorption of hydrated minerals in Ryugu is carefully examined. Finally, the validity of spectral sensitivity of ONC-T is also examined by reproducing a true color image of the Earth by composing multiband images taken during Earth swing-by in section 7-3.

7-1. Measurements of Reflectance of Mars

Multi-band observations of Mars were performed on May 24, 25, and June 7, 2016 in the cruising phase to examine the spectral sensitivity of ONC-T. Table 8 summarizes the geometric conditions at these observations. As shown in the table, the apparent diameters of Mars during the observations exceeded one pixel for ONC-T, and therefore it was possible to use the radiance coefficients measured in the pre-flight calibration to derive radiance [K2017]. Exposure times for each band are listed in Table 9. The exposure time settings were optimized after checking the first results, and thus more appropriate values were applied in the following observations. With respect to each shooting, images with zero-exposure time (i.e. smear images) were also obtained at nearly simultaneous timings. The signals obtained by ONC-T were converted to reflectance spectra by the following procedures. First, the smear image was subtracted from the raw image for each band. Following the subtraction, image data with signals in a digital number (DN) were converted to radiance for each band by applying the radiance coefficients and flat data shown in K2017. An image area enclosed by a square of size 20 pixels that contained Mars in its center was defined as ‘Mars area’. Similarly, an image area enclosed by a square of size 100 pixels with a center that was common with ‘Mars area’ was defined as ‘Total area’. A hollow square area obtained by subtracting the ‘Mars area’ from the ‘Total area’ was defined as ‘background (BG) area’. The averaged value of the ‘BG area’ was considered as background intensity. The background intensity was subtracted from each pixel of the ‘Mars area’. The total value of the background-subtracted ‘Mars area’ corresponds to the radiance of Mars. The reflectance of Mars was then deduced by dividing the radiance with reference solar irradiance at the Mars orbit (1.50 - 1.52 AU). The irradiance at the Mars orbit is calculated based on a reference solar spectrum developed by American Society for Testing and Materials (http://rredc.nrel.gov/solar/spectra/AM0/ASTM2000.html). Solar irradiance for each band is then calculated by averaging the irradiance spectrum by using the system efficiency for each band as a weight function (see K2017). The reflectance normalized at the v-band (550 nm) for the May 31 dataset is shown in Figure 14 (a) with black dots. Reflectance spectra based on ground observations by Singer (1973) are also shown with solid and dashed curves as references. The dashed and solid curves show spectra at dark and bright areas in Martian surface, respectively. Thus, the observed spectrum is expected to fall between these spectra since the present results are hemispherically averaged value. However, reflectance values in longer wavelengths (x- and p-bands) departed from the expected range. This was due to a temperature dependence of CCD sensitivity. Figure 13 shows the temperature dependencies of CCD sensitivity for various wavelengths provided by the manufacturer (E2V). Significant dependencies on temperature are clearly observed for the wavelengths. The radiance coefficients shown in K2017 corresponded to values at room temperature (24-28 °C). Conversely, CCD temperature during the observations of Mars was approximately −33.7 °C based on the house keeping (HK) data. This clearly indicates that a temperature correction is necessary to obtain true radiances. A spectrum on May 30 corrected by taking this effect into account is shown by the red dots in Figure 14 (a). The corrected spectrum falls within the expected range. Figure 14 (b) shows all three spectra after the correction.

Table 8. Geometric conditions at observations of Mars by ONC-T.

Date	Mars-Sun distance (AU)	Mars-HY2 distance (AU)	Mars-Earth distance (AU)	HY2-Mars-Sun Angle (deg)	Mars radius (pixels)	Rotational longitude (deg)
12:45 May 24, 2015	1.52	0.315	0.507	3.9	0.68	343
12:45 May 31, 2015	1.51	0.291	0.503	1.3	0.74	279
10:30 June 7, 2015	1.50	0.271	0.508	6.7	0.79	182

Table 9. Exposure times in a unit of [msec] for each band.

Date	ul	B	v	Na	w	x	p
May 24, 2015	43.5	16.4	16.4	32.8	16.4	21.8	43.5
May 31 and June 7	696	131	87.0	131	43.5	65.6	131

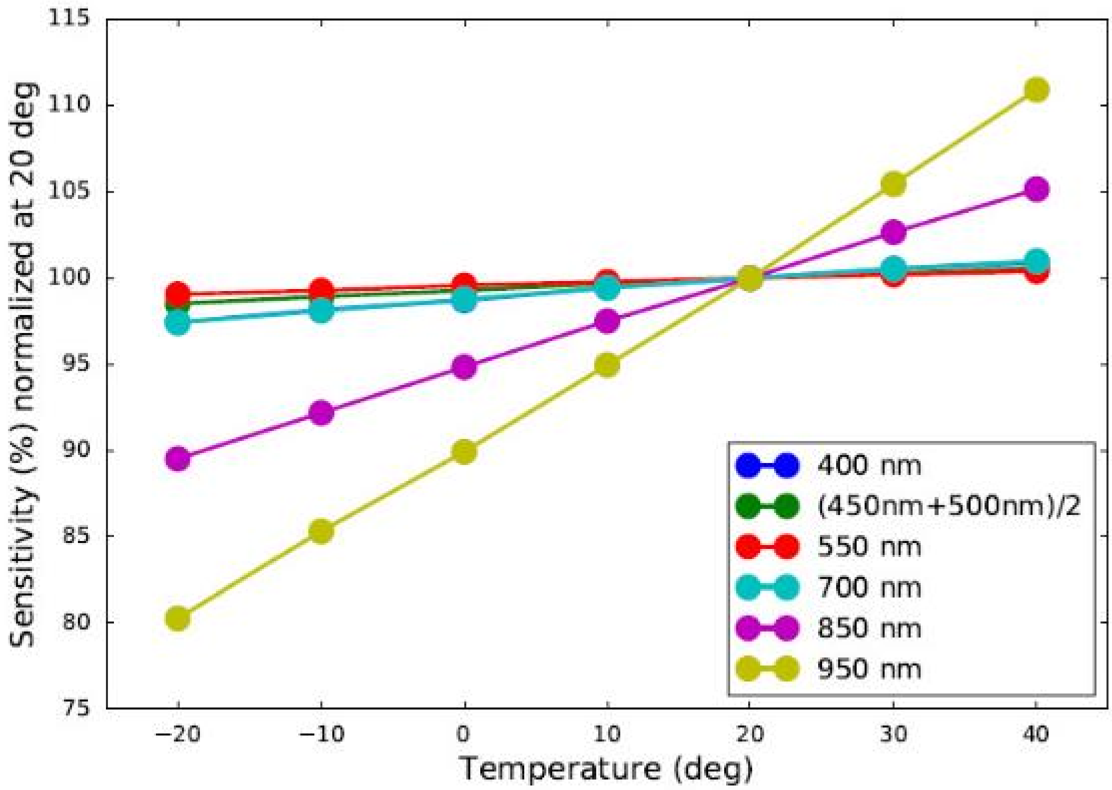

Figure 13. Temperature dependences of CCD sensitivity for various wavelengths provided by the manufacturer (E2V).

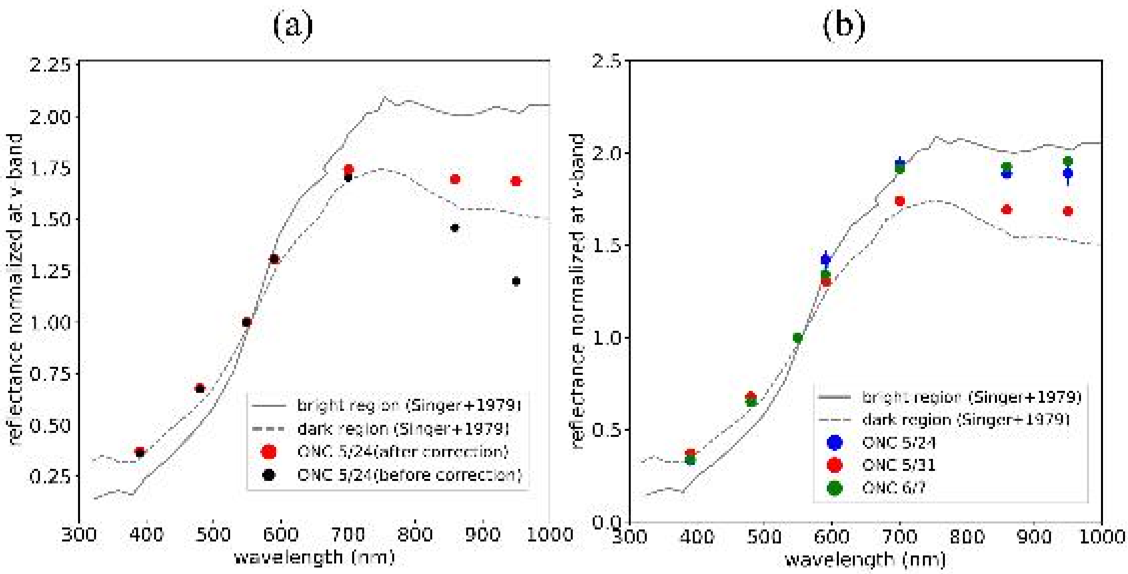

Figure 14. (a) Reflectance normalized at the v-band (550nm) for the May 31 dataset. Black (Red) dots show normalized reflectance without (with) the temperature correction. (b) Comparison among three days of observations (May 24, 31 and June 7) of reflectance spectra corrected for CCD sensitivity on temperature. The solid and dashed curves are spectra for bright and dark regions on Mars, respectively (Singer et al., 1973).

7-2. Comparison with SELENE/SP Lunar Reflectance Model

The lunar surface reflectance involves long-term stability (less than 1% variation during 1 million years, Kieffer (1997). Although recently Speyerer et al. (2016) reported that the time scale for 1% variation may be only 81,000 years, even this time scale is considerably longer than the mission time scales. Hence, the Moon is an ideal target for radiometric calibration of sensors in space once a reliable lunar reflectance and photometrical model are obtained. Spectral Profiler (SP) onboard SELENE (a Japanese Lunar orbiter) provided a global hyperspectral lunar reflectance and photometrical model (known as the SP model, Yokota et al., 2011), which enables the simulation of any lunar observation including a far side observation (Kouyama et al., 2016).

The ONC had an opportunity to observe the Moon on December 5, 2015 with a sufficient pixel size (approximately 20-pixel radius) for radiometric calibration after Hayabusa2's swing-by operation to obtain gravity assist to go to Ryugu using the Earth. Figure 15 shows an example of an observed lunar image captured with the v-band and its simulation image based on the SP model. The observed spatial distribution of brightness is simulated well; the correlation between observed and simulated images is higher than 0.99. At the observation, the sub spacecraft latitude and longitude was -56.37° and -96.25°, respectively, the observation distance corresponded to 764,658 km, and the phase angles was 59.3°. Gaussian smoothing with FWHM = 1.71 (see section 5) was performed in the simulated image to match the PSF of ONC-T.

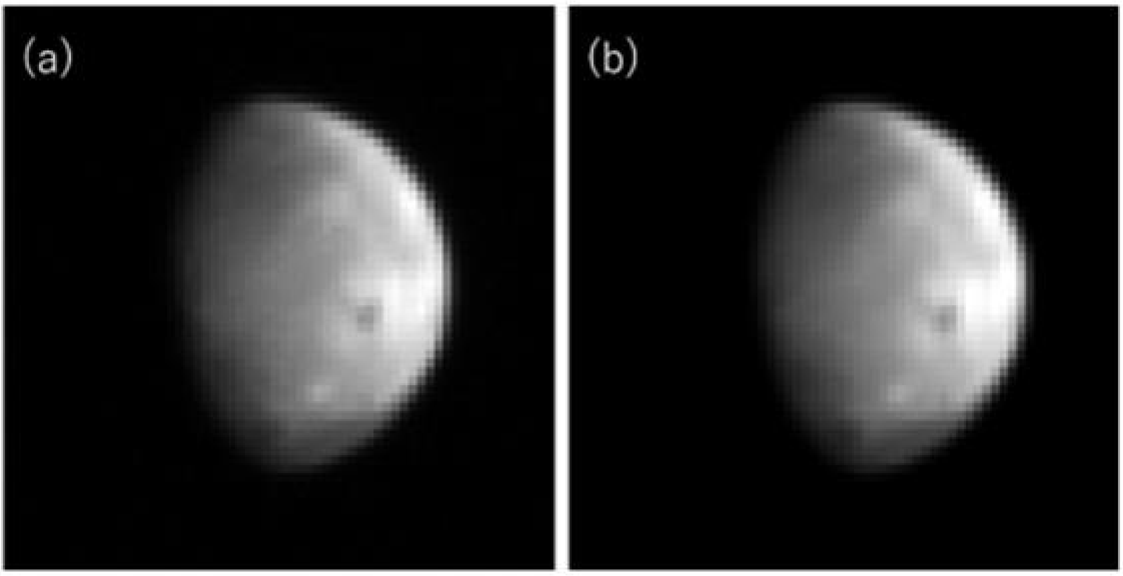

Figure 15. (a) Observed lunar image taken on December 5, 2015 (v-band) and (b) its simulated image based on the SP model by Kouyama et al. (2016).

Sensor sensitivity variations among ONC bands could be calculated through comparisons between observed and simulated lunar brightness at each band. Lunar irradiance I (W m^{-2} µm^{-1}) was used for the comparison, which is estimated as follows:

$$I = \sum_i r_i \, \omega_{pixel}, \qquad (6)$$

where i indicates i-th pixel included in Moon disk region and surrounding blurred region in each lunar image, r_i denotes radiance (W m^{-2} sr^{-1} µm^{-1}) at the i-th pixel, and ω_{pixel} denotes steradian of a pixel. Sensor sensitivity correction based on CCD temperature described in the previous section was performed to measure r_i (approximately -29.5 °C during the Moon observation sequence). The SP model covers a wavelength ranging from 512 nm to 1650 nm, and thus observed lunar images obtained with 549 nm, 700 nm, 859 nm, and 950 nm bands were used. Previous studies have confirmed that the reflectance from the SP model showed a darker trend in the short wavelength range (several tens %, Ohtake et al., 2013; Kouyama et al., 2016), and a correction with another lunar reflectance model was proposed for the SP model (Kouyama et al., 2016). In the present study, the ROLO model was used for the correction, which was developed from ground-based multi-spectral lunar observations and with an absolute brightness that has displayed good consistency (up to 10% discrepancy) with several satellite lunar observations in visible and near infrared wavelength range (Kieffer and Stone, 2005).

Measured irradiances of the observed and simulated values are listed in Table 10. With respect to absolute irradiance comparisons, the observed irradiances were ~15% brighter than those from the simulated images. However, because there is significant uncertainty in the absolute intensity calibration of the Kaguya spectral model, more thorough examinations are necessary for decisive conclusions for the accuracy of the absolute intensity calibration of the ONC-T (cf. Kouyama et al., 2016).

In contrast, irradiances normalized by 550 nm irradiance of observation and simulation exhibit good agreement (Figure 16); discrepancies less than 3%. This indicates that the relative sensitivities among the ONC bands did not vary from those at the ground-based experiment (K2017). In particular, discrepancies among the three bands (v-, w, x-bands) used for detecting the spectral absorption around 0.7 µm caused by hydrated minerals in the surface of Ryugu are 0.07 - 1.4 % (see Table 10). Figure 16 also shows observed irradiances without sensor sensitivity correction based on CCD temperature. The distribution without the correction differed from the simulated spectrum much more than the corrected one, which indicated that in a manner similar to the Mars observation, the sensitivity correction based on CCD temperature is essential to measure a target color ratio.

Although relative spectral sensitivities among ONC-T bands were verified in the analyses discussed above, the accuracy of flat-field needs to be examined with different analysis. In fact, we conducted flat-field measurements using a portable flat light source immediately after the flat-field measurements with an integrating sphere discussed by K2017 before camera assembly to the spacecraft, during the final integration test for the Hayabusa2, and during pre-flight health check at Tanegashima launch site. The result of this series of measurements with the portable flat light source suggested that a slight shift in the vignetting pattern in the FOV. However, it was difficult to judge this small change in a flat field pattern is real or artifact due to some change in our measurements system, since only one band of image was taken because of the lack of time. There was no opportunity to examine this uncertainty until the lunar measurements. In order to take advantage of this opportunity, we took images of the Moon both at the center of FOV (the center image) and near a corner of FOV (the corner image). The moon observations revealed a deviation in a flat field from its reported value in K2017. Figure 17 shows the ratio of irradiances estimated from two different lunar images by using equation (6). The center image is the same one that used in the comparison with the lunar reflectance spectral model. If a flat correction by using the values reported in K2017 were sufficient, then the ratio of irradiances estimated from these two images should be unity in all the bands. However, as shown in Figure 17, irradiance estimated from the corner image by using the flat data reported in K2017 was ~10% brighter than that of the center image for all bands except for the ul-band. This fact suggests that a flat field for each band deviated from that obtained by using an integrating sphere in a laboratory (K2017). These deviations are as almost identical for all bands except for the ul-band. Thus, a slight shift in the front hood position during disassembly and assembly works of Hayabusa2 prior to the launch was suspected. This was examined using data taken in the portable flat light source measurements mentioned above. Figure 18 (a) shows the normalized image of the light panel captured on Dec 2014 at Tanegashima (Launching site). The image was captured only at the v-band, and the flat distribution appeared similar to that reported in K2017 (see Fig. 10 of K2017). Figure 18 (b) shows ratio between the normalized flat (Figure 18 (a)) and that shown in K2017. This clearly showed a deviation of the flat distribution, especially in the corners of the image. In a corner of small (large) X and Y, approximately +10 % (-10 %) increase (decrease) in the flat was evident. This type of variation can occur when the center of the front hood shifts towards x-direction and y-direction relative to the original position. Thus, it was assumed that this variation in the flat field was common across all bands and did not suffer from any additional changes during the launch and the initial cruising phases. In Figure 16, the ratio of lunar irradiances recalculated by using Figure 18 (b) as a correction factor is also shown by blue circles. This new result shows the ratio of irradiances estimated by using two images close to unity (within 2%) for all the bands except for the ul-band. Furthermore, the accuracy of the flat correction becomes within 1% among the three bands (v-, w-, and x-bands) if the ratio shown in Figure 16 are normalized by the value at v-band. Therefore, new flat fields that were corrected from those reported in K2017 by using the factor shown in Figure 18 (b) were considered to be better flats for all the bands except for the ul-band. These flats are probably the best flat we can estimate at this point and thus defined as provisional reference flats prior to arrival at Ryugu.

Here, it is noted that the increased error in the flat-field calibration obtained for the ul-band (Fig. 17) is due to a different type of stray light. Details for this stray light are described in Section 8-2.

Table 10. Comparison of disk-integrated spectral irradiances (μW m^{-2} μm^{-1}) of the Moon for different bands between actual ONC-T observation and simulation based on the Kaguya model.

Bands	v	w	x	p
Observation	349	351	269	247
Simulation	313	315	238	215
Observation/Simulation	1.115	1.114	1.130	1.149
Ratio normalized with v-band	1.000	0.999	1.014	1.030
δI_i (%)	-	0.07	1.4	3.0

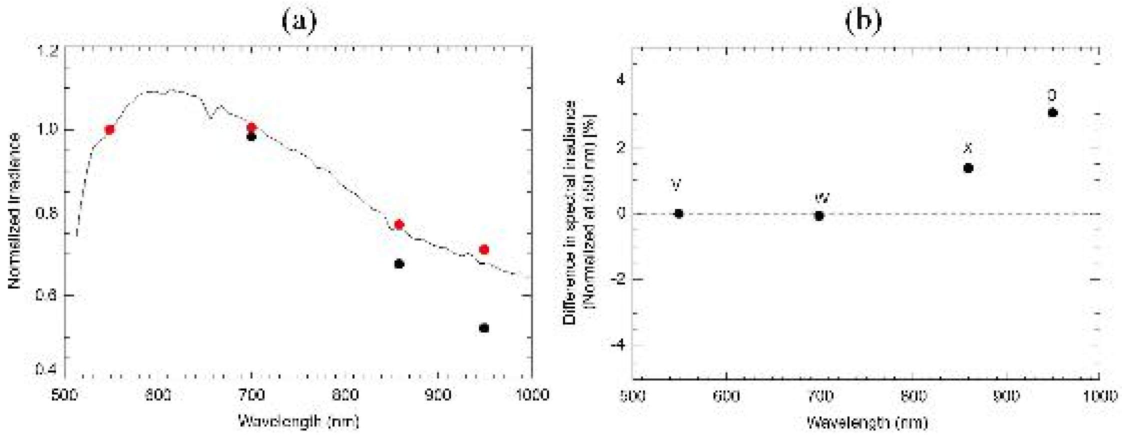

Figure 16. (a) Comparison of normalized irradiances between observed lunar images (red dots), and simulated irradiance spectrum based on SP model corrected with ROLO model (solid line). Observed irradiances without sensor sensitivity correction based on CCD temperature are also plotted (black dots). Irradiance at 550 nm is used for the normalization of each irradiance plot.

(b) The ratio of irradiance observed by ONC-T to those by ROLO-corrected Kaguya (SP) model normalized at v-band.

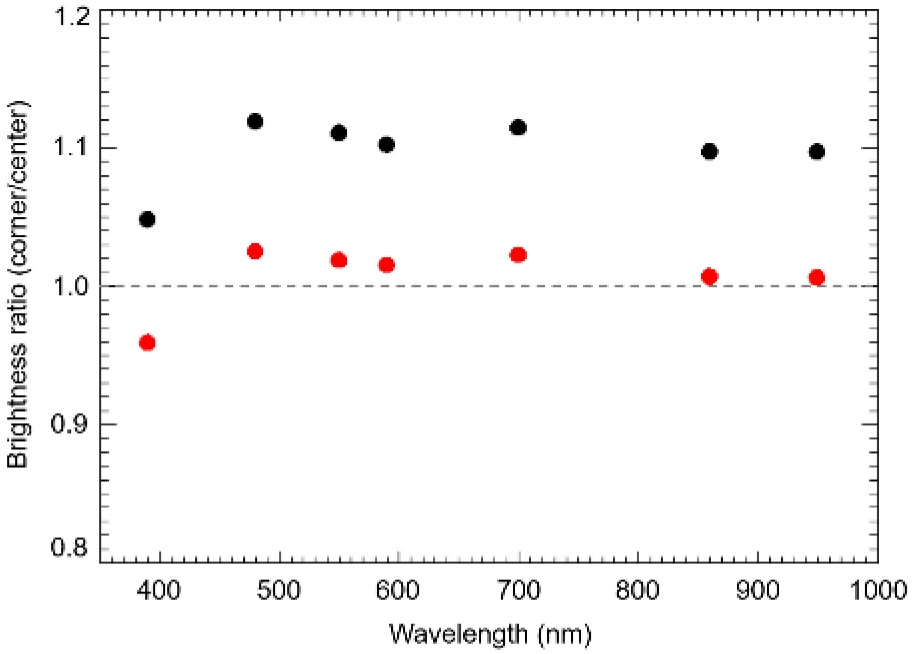

Figure 17. The ratio of the irradiances estimated from lunar image near corner of the FOV to that at the center of FOV. The deviation of this ratio from unity is a measure for the inaccuracy of our flat correction of ONC-T. Black and Red dots show those calculated by using sensitivity flat data reported by K2017 and newly defined in the present study taking into the account the affect of slight change in hood position between the laboratory calibration and the last assembly before the launch.

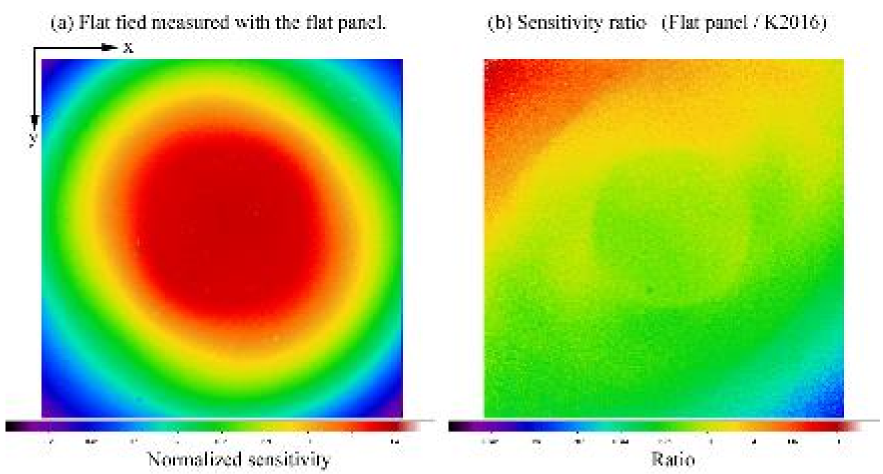

Figure 18. (a) Normalized sensitivity flat measured with the flat panel. (b) Ratio between the normalized flat and that shown in K2017.

7-3. Reproduction of a true color image using sensitivity calibrated multi-band dataset.

During the Earth swing-by phase, ONC-T captured multi-band images of the Earth. Images of six bands (ul-, b-, v-, w-, x-, and p-bands) were successfully obtained. The center wavelengths of each band lies between 390 nm and 950 nm [see K2017] including the most part of visible range (360-780nm). Obtained signal values in each band [DN/sec] were converted to radiance in units of $\mathrm{Wm^{-2}sr^{-1}nm^{-1}}$ by applying flat and radiance coefficients measured with an integrating sphere in pre-flight calibration [K2017]. By combining these calibrated multiband images, a spectrum of radiance flux corresponding to each location in the Earth's image was obtained. The spectrum of the radiance covering the visible range could be converted to (R,G,B) values in an sRGB color space [International Standard, IEC 61966-2-1, 1999]. This suggests that the natural color of an object could be reproduced as a color image by using a multiband dataset.

The first step involves registration of the Earth's images in each band. Although all the bands share common optics and the CCD sensor except for interference filters [details in K2017], the focal length (i.e., field of view) may be slightly different for each band due to a chromatic aberration of the optics. For this reason, a position and a magnification of the Earth's images taken at each band were deviated by sub-pixel to a pixel of distance from each other. In order to minimize this effect, a registration method that considered shift, rotation, scaling, and affine deformations [Leprince et al., 2007; Matsuoka and Kodama, 2011; Kouyama et al., 2016] were applied. Following the registration, a set of (R,G,B) values were calculated in a 24-bit true color system. A radiance value of the i-th band at the j-th pixel was defined as $I'_{\mathrm{j}}\ (\lambda_{\mathrm{c,i}})$ [$\mathrm{Wm^{-2}sr^{-1}nm^{-1}}$], where $\lambda_{\mathrm{c,i}}$ denotes a center wavelength of the i-th band. This radiance spectrum with discrete wavelengths was linearly interpolated and extrapolated to have values at wavelengths with regular intervals (1 nm) between 360 nm and 780 nm. This interpolated and extrapolated radiance spectrum corresponding to the j-th pixel is represented as $I_{\mathrm{j}}\ (\lambda)$. This radiance spectrum is used as a spectroscopic distribution function to derive three stimulus values, X, Y, and Z in CIE1931 color system as follows:

$$\mathrm{X_j} = \mathrm{k}^{-1} \int_{360nm}^{780nm} \bar{x}\,(\lambda)\, I_{\mathrm{j}}\,(\lambda)\, \mathrm{d}\lambda\,,$$

$$\mathrm{Y_j} = \mathrm{k}^{-1} \int_{360nm}^{780nm} \bar{y}\,(\lambda)\, I_{\mathrm{j}}\,(\lambda)\, \mathrm{d}\lambda\,, \qquad (7)$$

$$\mathrm{Z_j} = \mathrm{k}^{-1} \int_{360nm}^{780nm} \bar{z}\,(\lambda)\, I_{\mathrm{j}}\,(\lambda)\, \mathrm{d}\lambda\,,$$

where,

$$\mathrm{k} = \int_{360nm}^{780nm} \bar{y}\,(\lambda)\, I_{\max}\,(\lambda)\, \mathrm{d}\lambda \qquad (8)$$

and $\bar{x}(\lambda), \bar{y}(\lambda)$, and $\bar{z}(\lambda)$ are color matching functions in the CIE1931 color system [Wyszecki and Stiles, 1982]. Additionally, $I_{\max}(\lambda)$ in the equation corresponds to the interpolated and extrapolated radiance spectrum of a pixel where brightness in a grayscale level is maximum for all pixels. The stimulus values are then converted to a set of (R, G, B) values in sRGB color space by using the following expression:

$$\begin{pmatrix} \mathrm{R_j} \\ \mathrm{G_j} \\ \mathrm{B_j} \end{pmatrix}_{\mathrm{sRGB}} = \begin{pmatrix} 3.2406 & -1.5372 & -0.4986 \\ -0.9689 & 1.8758 & 0.0415 \\ 0.0557 & -0.2040 & 1.0570 \end{pmatrix} \begin{pmatrix} \mathrm{X_j} \\ \mathrm{Y_j} \\ \mathrm{Z_j} \end{pmatrix}. \quad (9)$$

The obtained set of (R,G,B) values are gamma-corrected by using the following rules:

$$\mathrm{R'}_{\mathrm{j},sRGB} = \begin{cases} \mathrm{R_{j,sRGB,}} \times 12.92 & if\ \mathrm{R_{j,sRGB}} \leq 0.0031308 \\ 1.055 \times (\mathrm{R_{j,sRGB}})^{\frac{1}{2.4}} - 0.055 & if\ \mathrm{R_{j,sRGB}} > 0.0031308 \end{cases}$$

$$\mathrm{G'}_{\mathrm{j},sRGB} = \begin{cases} \mathrm{G_{j,sRGB}} \times 12.92 & if\ \mathrm{G_{j,sRGB}} \leq 0.0031308 \\ 1.055 \times (\mathrm{G_{j,sRGB}})^{\frac{1}{2.4}} - 0.055 & if\ \mathrm{G_{j,sRGB}} > 0.0031308 \end{cases} \quad (10)$$

$$\mathrm{B'}_{\mathrm{j},sRGB} = \begin{cases} \mathrm{B_{j,sRGB}} \times 12.92 & if\ \mathrm{B_{j,sRGB}} \leq 0.0031308 \\ 1.055 \times (\mathrm{B_{j,sRGB}})^{\frac{1}{2.4}} - 0.055 & if\ \mathrm{B_{j,sRGB}} > 0.0031308 \end{cases}.$$

Finally, each color value is encoded to 8-bit digitized values (0-255) by the following expression:

$$\begin{pmatrix} \mathrm{R_j} \\ \mathrm{G_j} \\ \mathrm{B_j} \end{pmatrix}_{\mathrm{sRGB\_8bit}} = \mathrm{int}\left(255 \times \begin{pmatrix} \mathrm{R'_j} \\ \mathrm{G'_j} \\ \mathrm{B'_j} \end{pmatrix}_{\mathrm{sRGB}} \right), \quad (11)$$

where ‘int( )’ denotes rounding to the nearest integer. The procedure to convert stimulus values (X, Y, Z) to sRGB values is based on an International Standard [IEC 61966-2-1, 1999]. A true color image was obtained by applying the procedure to all pixels. Figure 19 shows the result of this color image processing applied to Earth’s images captured during the Earth swing-by. The resolution of the image corresponded to 512 pixels × 512 pixels trimmed from the original 1024 pixels×1024 pixels data. In the obtained true color image, the continent of Antarctica, a part of the South African continent, Madagascar island, and the Australian continent with a swirling cloud pattern are identified. The color features in the Earth’s surface appeared to be natural, supporting that flat and radiance coefficients measured in the pre-flight calibration [K2017] are accurate in the visible range after the launch.

The accuracy of co-registration was also examined by creating a map of a certain feature in the spectrum. For example, a Normalized Difference Vegetation Index (NDVI) was calculated using the same Earth images. The NDVI is an index that indicates the distribution and activity of vegetation on the Earth's surface and is defined as: $\mathrm{NDVI} = (R_x - R_w)/(R_x + R_w)$, where R_x and R_w denote reflectance of the Earth's surface at wavelengths corresponding to x-band and w-band, respectively [e.g., Benedetti and Rossini, 1993]. Figure 20 shows a distribution of NDVI calculated by using x-band and w-band images captured by the ONC-T camera during the Earth swing-by. A few distinct areas that indicate rich vegetation relative to the ocean or the Antarctic continent are evident in this image. Such successful co-registration and ratio map generation suggests that the ONC-T camera is capable of capturing important spectroscopic features, such as UV slope and absorption band at approximately 0.7 μm of Ryugu, in a similar manner.

Figure 19. A color image of the Earth reproduced by multiband images captured by the ONC-T camera during the Earth swing-by.

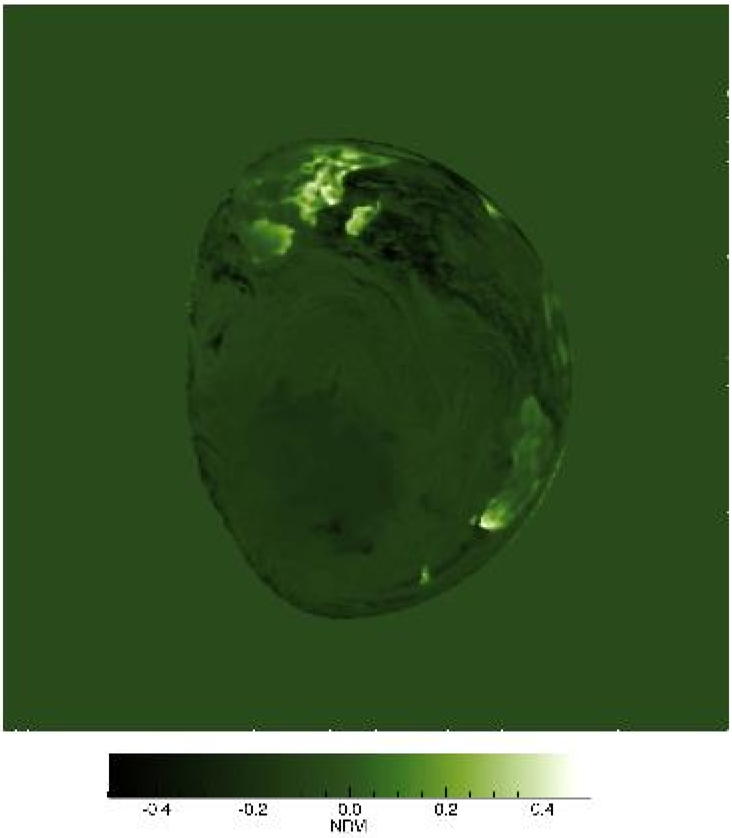

Figure 20. Spatial distribution of NDVI calculated by using x-band and w-band images captured by the ONC-T camera during the Earth swing-by.

8. Stray Light Analysis

Attention was specifically focused on the stray light of the ONC-T camera. This was because very subtle absorption features, such as the 0.7μm band of serpentines (only up to approximately 3% of change in reflectance as indicated by Vilas and Gaffey, (1984)) constitute important science observation targets for the camera. In this section, trends and countermeasures of two types of stray light found in ONC-T observations during flight are described.

8-1. "Radiator" stray light

Following the launch, observations indicated that the ONC-T camera was susceptible to considerably strong stray light when the orientation of the spacecraft was within a certain range of conditions. However, the stray light is negligible beyond this range (< 1 DN/shot) for spectroscopic observations of Ryugu. Observations are planned to conduct within the negligible stray light range at Ryugu. Thus, the stray light would virtually not exert an influence on the spectroscopic or morphologic observations of Ryugu. However, there may occasions when we have to conduct observations under the stray light conditions among a great variety of operations of Hayabusa2 around an unexplored asteroid. Thus, it is necessary to carefully investigate the stray light patterns and conditions and prepare to analyze image data with stray light prior to arrival at Ryugu.

Nevertheless, the findings indicated that the stray light was independent of the filter. That is, the light displayed the same intensity and pattern irrespective of filter selection. This indicated that it was unlikely that the stray light originated from the fore optics. As discussed in the following section, this stray light occurred when sunlight hit the area around the radiator to cool the CCD of ONC-T. Thus, the stray light was termed as "radiator" stray light in this study. Here, it should be noted that other significant stray lights were not detected for the ONC-T camera following the launch.

The typical pattern of the radiator stray light is shown in Figure 21. The radiator stray light is more intense around the corner of (X, Y)=(1023, 1023) and less intense around the corner of (X, Y)=(0, 0). The stray light image is binned by 128x128 pix (8x8 tiles) to smooth the noise fluctuations and to obtain general trend in the variation in the maximum intensity of stray light as a function of a location within FOV (Fig. 21b). This was followed by evaluating the intensity of each stray light image with the highest intensity tile, i.e., (binned X, binned Y)=(7, 7). This suggests that the radiator stray light had a less influence at the center of the FOV.

The spatial patterns of stray light of different images were very similar to each other in most cases, but the intensity was highly dependent on the attitude of the spacecraft with respect to the Sun. The intensity of radiator stray light was assessed with respect to changes in the spacecraft attitude from June 2015 to July 2016. The intensity of radiator stray light was classified into the following three types: (1) negligible stray light less than 1 DN/shot, (2) weak stray light less than 0.1% of the light from typical asteroid surface, and (3) strong stray light more than 0.1% of the light from typical asteroid surface. It should be noted that even when strong stray light was present, the intensity did not exceed 10% of the intensity of an object. Based on the phase function by Ishiguro et al. (2014), we estimated the adequate exposure time for Ryugu during the period of the intensive global observations. The typical exposure time for the three bands (v, w, and x-bands) used for the detection of 0.7μm absorption is found to be 0.264 sec or less. It was assumed that the intensity of light from asteroid is 2500 DN during the typical exposure time 0.264 sec for the three bands. Thus, the above classification was equivalent to condition (1) < 3.8 DN/sec, condition (2) < 9.5 DN/sec, and condition (3) > 9.5 DN/sec, respectively. When the stray light is intense (i.e., condition (3)), the observations of subtle absorption features around 0.7 μm will be interfered significantly.

The spacecraft attitude with respect to the Sun could be defined by two parameters, namely X_{PNL} and Y_{PNL}, which correspond to the angles of the Sun to $+X_{SC}$ plane and $+Y_{SC}$ plane of the spacecraft, respectively (Figure 22(a)). Here 90° - X_{PNL} is also equal to the angle of the Sun with respect to the $+X_{SC}$ axis.

$$\boldsymbol{s} \cdot \boldsymbol{X}_{SC} = \sin X_{PNL}\,, \;\; \boldsymbol{s} \cdot \boldsymbol{Y}_{SC} = \sin Y_{PNL}, \qquad (12)$$

where $\boldsymbol{s}$ is a unit vector from the spacecraft to the Sun in the spacecraft coordinate system. Figure 22(b) summarizes the intensity classification of radiator stray light in the $X_{PNL} - Y_{PNL}$ plane. It is possible to avoid the radiator stray light by selecting the spacecraft attitude with respect to the Sun. It should be noted that the attitude conditions (1) and (2) will not interfere very much the detection of the 1 – 3% absorption of the 0.7μm band of serpentines. Furthermore, the similarity in the spatial pattern of radiator stray light among images at nearby attitude conditions suggests the possibility for correction of the stray light. However, this type of correction would necessitate further data on stray light.

In order to avoid strong stray light, it is necessary for the spacecraft to twist around the axis Z_{SC}. The reference spacecraft attitude used in this study is defined as the attitude where the $+Z_{SC}$ normal vector points to the Sun and the solar angle Y_{PNL} and X_{PNL} were zero. The target spacecraft attitude can be given with two rotation angles with the orders of rotations specified owing to the nature of spherical coordinate system. In this study, we specify the angle φ by which the spacecraft is twisted around the Y_{SC} axis first and the angle γ by which spacecraft is twisted around the Z_{SC} axis second. Here the Y_{SC} twisting angle φ is equal to angle of Sun-Probe-Earth (SPE) because the high-gain antenna (Z_{SC}) should point to the Earth during observation. That is, the rotation matrix from the reference spacecraft attitude is

$$M = \begin{bmatrix} \cos\varphi\cos\gamma & \sin\gamma & -\sin\varphi\cos\gamma \\ -\cos\varphi\sin\gamma & \cos\gamma & \sin\varphi\sin\gamma \\ \sin\varphi & 0 & \cos\varphi \end{bmatrix}. \quad (13)$$

After such an operation, the spacecraft-to-Sun vector (0,0,1) at the reference spacecraft attitude is rotated as

$$\tilde{\boldsymbol{s}} = M\boldsymbol{s} = \begin{bmatrix} -\sin\varphi\cos\gamma \\ \sin\varphi\sin\gamma \\ \cos\varphi \end{bmatrix}. \quad (14)$$

Thus, the relationships between X_{PNL} and the operational angles, φ and γ and that for Y_{PNL} are derived as

$$-\sin\varphi\cos\gamma = \sin X_{PNL}\,, \sin\varphi\sin\gamma = \sin Y_{PNL}. \quad (15)$$

Figure 23 shows the radiator stray light intensity as a function of the twisting angle γ. The stray light decreased dramatically at approximately γ = -7 deg and was negligible at γ < -10. The dependence of stray light strength on γ is very similar for different solar phase angle (φ). Stray light at γ < -10 deg is negligible when γ < -10 deg for all the solar phase angles we have measured. Thus, the radiator stray light could be avoided through twisting the spacecraft to γ < -10 deg. This evaluation has not been completed yet; test for additional attitudes such as $0 < X_{PNL} < 15$ deg are planned. However, data obtained to-date strongly suggest that the trend of stray light occurrence would be similar for the uninvestigated conditions.

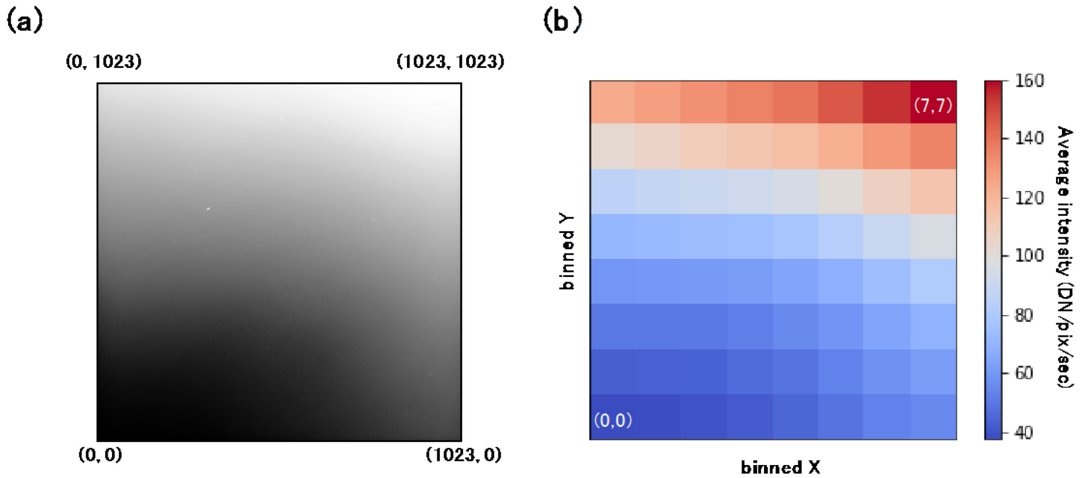

Figure 21. A typical pattern of the stray light (image no. 01884; contrast is stretched with histogram equalization). (a) The raw image and (b) the binned image with 128x128 pix tiles. The stray light intensity is evaluated at the highest intensity tile, i.e., (binned X, binned Y)=(7, 7).

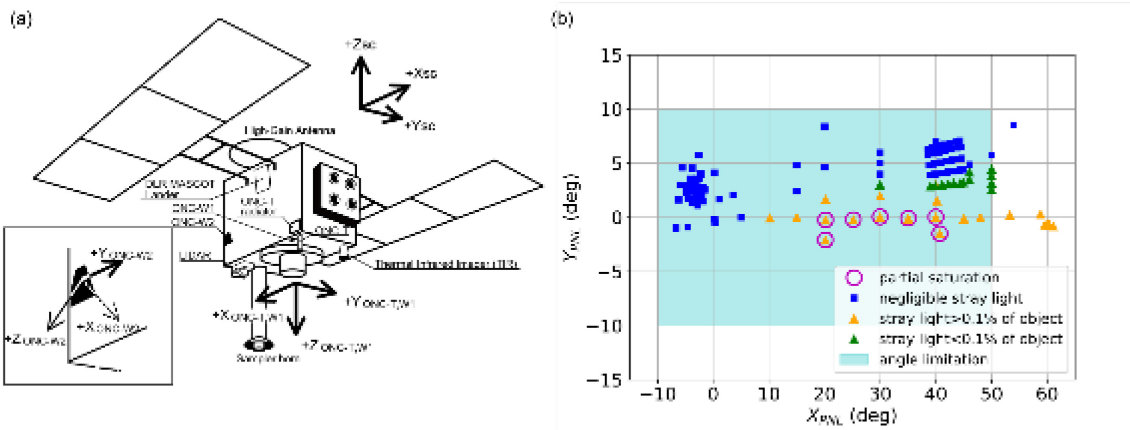

• Figure 22. Radiator stray light occurs as a function of the angle of the sun to the $+X_{SC}$ plane and $+Y_{SC}$ plane (X_{PNL} and Y_{PNL}). (a) The definition of the spacecraft coordinate system. The ONC is placed close to $+X_{SC}$ plane. (b) The intensity classification of radiator stray light: negligible stray light (blue), weak stray light (green), and strong stray light (yellow). Due to long exposure times (5.57 sec), a few stray light images were partially saturated (magenta circles). There is an angle limitation for science observations, shown as light-blue hatch, owing to the thermal condition of the spacecraft, but the spacecraft could temporarily take attitudes outside the limitation.

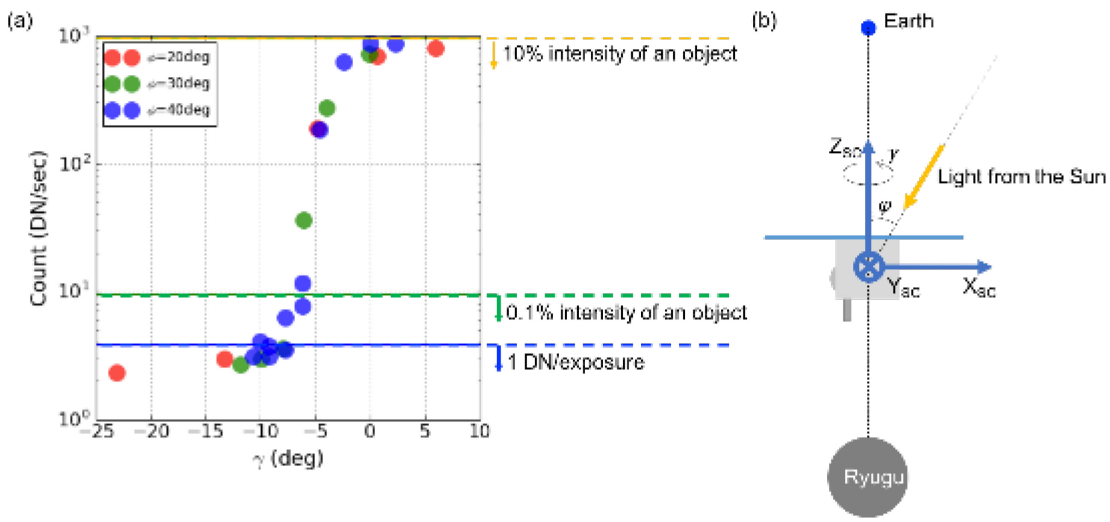

• Figure 23. (a) The intensity of radiator stray light in the block with the strongest stray light in FOV as a function of the twisting angle γ measured from the standard attitude for different Sun-Probe-Earth (SPE) angles (20, 30, and 40 degrees). The radiator stray light could be avoided by twisting the spacecraft around the Z_{SC} axis. Exposure time (0.264 s) for 2500 DN value for Ryugu images is used. When less than 1 DN of stray light is received (blue dashed line), it is undetectable. When the intensity of the stray light corresponds to 0.1% of Ryugu surface brightness (green dashed line), it is detectable but does not become a significant obstacle in the detection of an absorption band with 1% of strength. (b) The geometric relation among the Sun, asteroid Ryugu, and spacecraft Hayabusa2. The angle φ is the solar phase angle. The angle γ is angle around the Z_{SC} axis measured from the reference attitude where the $-Z_{SC}$ axis is pointing to the asteroid and $+Z_{SC}$ axis is pointing to the Sun.

8-2 "FW roundabout" stray light

As mentioned in Section 7-2, the increased error in the flat-field calibration obtained for the ul-band (Fig. 17) is due to a different type of stray light that occurred in laboratory calibration measurements using an integrating sphere. This stray light comes to bottom side of the CCD via a path going around the filter wheel (FW) from the lens tube holding the fore optics. Although light that reaches the ONC-T optics with small incident angles with respect to its optical axis does not go through this roundabout path, some of the large-incidence-angle light would reach CCD through this roundabout path. We termed this stray light as "FW roundabout stray light". Because its strength is independent of the choice of filter, the intensity of this noise relative to the signal through the filter is greater for a band with a lower signal level. Also, this stray light is pronounced particularly in integrating sphere measurements because light irradiated to the examined camera in such tests contains light with very large incidence angles. In fact this stray light becomes negligible for light with small incident angles; integrating sphere measurements from a distance to fit within the FOV of ONC-T exhibit no stray light. Furthermore, because integrating sphere has much lower color temperature than the Sun, the signal-to-noise ratio (SNR) for shorter wavelength bands becomes lower in integrating sphere measurements. Consequently, the ul-band, the darkest and shortest wavelength band among the 7 filters of ONC-T, ended up suffering from the strongest stray light effect in its flat-field calibration. Actually, because rather strong roundabout stray light was found during an early test of ONC-T in a laboratory, an additional wall was installed between the FW and the CCD of ONC-T to block this stray light. However, because of the limitation for the design change, this stray light could not be removed completely. Nevertheless, comparison of the Moon images between the center of FOV and a corner of the FOV, where FW roundabout stray light is expected to occur, indicate that the intensity of this stray light is less than 2% for integrating sphere measurements for all the filters other than ul-band. This would be a very important property for observations at low altitudes at Ryugu where ONC-T will receive light from large incidence angles. Furthermore, the FW roundabout stray light is much weaker for the actual Sun light and its reflected light from C-type asteroids, which have flat reflectance spectra. Thus, flat field calibration for bands others than ul-bands are better than 2% both for global observations from the Home Position (20km from Ryugu) and lower altitude observations. The error in flat field calibration for the ul-band is about 10%, but FW roundabout stray light for ul-band is less than 2% for HP observations, where no large incidence angles of light reaches the camera from Ryugu. Thus, the accuracy of the flatness of ul-band images may be corrected down to less than 2% when a better flat-field calibration image is obtained. Obtaining such calibration image is beyond the scope of this study but is among the high-priority objectives of our flight calibration during the rest of cruising phase of Hayabusa2 before arriving at Ryugu.

9. Summary of the inflight calibration results and implications for Ryugu observations.

In this section, we summarize our inflight calibration results in this study and discuss the accuracies of our observations of asteroid Ryugu based on the inflight calibrated data. More specifically, we discuss the accuracy of topography and morphology with W1 and W2 in the section 9-1 and the possibility of observing spectroscopic features on Ryugu with ONC-T in section 9-2.

9-1. ONC-W1 and W2

In the study, the validity of the distortion coefficients measured in pre-flight calibration for W1 and W2 cameras was verified by using post-launch star images taken on Feb 19, 2015 (W1) and Dec 11, 2014 (W2). The star images also provided precise pixel resolution and effective fields of view for both cameras. The measured and verified values would be used for close-up images of surface structures of Ryugu captured during the touchdown sequence. The accuracy of the distortion correction was confirmed to be less than a pixel for both cameras. This means accuracy in apparent angle measurements from an image is better than the mean pixel resolution (0.0681 and 0.0673 degrees/pixel for W1 and W2) (see Section 3). For example, this corresponds to a horizontal distance of ~12cm on the surface of Ryugu for observations from 100m of altitude.

Signal levels in Earth's images captured during the swing-by phase were also confirmed to be consistent with values predicted by using the pre-flight calibration data and Earth's albedo. This indicates that severe degradations did not occur in the sensitivities of W1 and W2 during the launching procedure.

9-2. ONC-T

The PSF was evaluated using a wide-band image with 23 stars. Analysis result indicates that the PSF did not degrade from that reported in K2017 within an area defined by $R < 580$ pixels where R denotes a distance from the center of the image in pixels. The PSF outside this area was slightly higher than 2 pixels. This increase in PSF is due to the extended hood, and is consistent with optical calculation. Furthermore, the PSF in most parts of the field of view (within an inscribed circle of FOV) was confirmed to be sufficiently small, and thus, no negative effects are expected for the global observation from a home position (~20km from the asteroid).

Distortion coefficients for the ONC-T camera were also determined by analyzing the star images captured during the inflight observation. As shown in section 6, the accuracy of the distortion correction with these values was confirmed to be ~ 1/10 pixel size over the entire FOV. The fact that the level of distortion was the same as or better than the AMICA of Hayabusa (Ishiguro et al., 2010), shape models with a similar accuracy for Itokawa (e.g., Demura et al., 2006) could be created for Ryugu with images taken with ONC-T of Hayabusa2.

Multi-band observations of Mars and the Moon were performed for a radiometric calibration of the ONC-T. The signal in the image of the Moon was converted to radiance for each band by using radiometric coefficients as reported in K2017. This was followed by computing the irradiances by the Moon at the location of Hayabusa2 for each band and comparing the same with that predicted by SELENE/SP Lunar Reflectance Model. In a similar manner, the spectrum of relative reflectance of Mars normalized at the v-band was also calculated and compared with previous results by ground observations. The comparisons indicated that observed spectra of a relative irradiance (Moon) and radiance (Mars) normalized at the v-band were consistent with the model and ground-based observations if a temperature dependence of CCD sensitivity was adequately accounted. In these analyses, the temperature dependences of CCD sensitivity for various wavelengths provided by the CCD manufacturer (E2V) were applied for data correction. However, it was necessary to perform more precise multi-band observations in Ryugu using the measurements of the temperature dependencies for the flight model (FM). For example, observation of a standard star with known flux by changing the CCD temperature during the cruising phase of Hayabusa2 is a way to quantify the temperature dependence of CCD sensitivity. The Moon observation revealed that normalized irradiances by each 550 nm irradiance of observation and simulation exhibit good coincidences with discrepancies less than 3%. In particular, the discrepancies become less than 1.4% among three bands (v-, w, x-bands) which are essential for detection of the spectral absorption caused by hydrated minerals such as supertine in the surface of Ryugu. The depth of the 0.7-um absorption can be defined by using signals from v-, w-, and x-bands as

$$d_{a=}1-\frac{3.1R_w}{1.6R_v+1.5R_x}, \qquad (16)$$

where, $R_v, R_w,\ and\ R_x$ are the reflectance of an asteroid observed with v-, w-, and x-bands (e.g. Kameda et al., 2015). In this case, the error of 0.7-um absorption is calculated to be 0.68% from the error propagation law. This fact suggests possibility for detection of the spectral absorption with 3% depth caused by hydrated minerals on the surface of Ryugu with SNR higher than 4. Although, the uncertainty in p band does not have direct influence on the detectability of the 0.7um absorption band, discrepancy between ONC-T observation and Kaguya model at the p band has rather large (~3%, see Table 10). This would suggest that the temperature dependence of p-band sensitivity may have large uncertainty. One possibility is a kind of individual difference in manufactured CCD chips. Thus, further investigation will be needed for higher accuracy in p-band.

Flat fields modified from those reported in K2017 using flat panel measurement immediately before the launch exhibits accuracy better than 2% for all bands except for the ul-band. This uncertainty in the flat field could causes errors in estimation of surface topography of Ryugu when photoclinometric method is applied. However, the magnitude of estimation error due to this level of flatness error is relatively small. For example, errors in inclination is estimated to be 1.1 degrees in a typical observation (45 degrees of topographic inclination and alignment of Zsc to the Sun are assumed) if Lambertian surface is assumed. Although the good reproduction of light intensity of the Moon in the FOV center and a corner strongly suggests that this flat field calibration corrected with the portable light source is sufficient for most data analysis, the inflight validation of flat field is limited to this example. Thus, there is room for improvement in accuracy with further investigation of flat field. Such additional investigation may be possible when Hayabusa2 can obtain close-up images of Ryugu.

Inflight observations also revealed the existence of the radiator stray light under certain conditions of spacecraft attitude. The intensity of the stray light was highly dependent on the attitude of the spacecraft with respect to the Sun. In particular, the radiator stray light becomes negligibly weak outside this condition. Thus, controlling the attitude of the spacecraft prior to the multi-band observation of Ryugu is necessary to reduce the radiator stray light. Additionally, observations indicated that the spatial patterns of stray light in the FOV do not change very much. The pattern appears to be similar to each other among different images taken at similar spacecraft attitudes. This fact suggests that this component of the stray light could be removed by appropriate image processing if the relationship between the stray light pattern and the attitude are accurately quantified. It is necessary to investigate the stray light patterns and conditions more carefully to analyze this type of image data with stray light prior to arrival at Ryugu.

10. Conclusion

In this study, image data obtained after launch was used to conduct a series of inflight calibrations for the ONC onboard Hayabsua2 for scientific observations of asteroid Ryugu.

First, PSF and distortion correction parameters were obtained using star field images, which provided virtually perfect point-source light. The results of the analysis indicate that both PSF and distortion after launch were the same within the error of the analyses. That is, they were not significantly influenced by the launch. The error of distortion correction was estimated as less than a pixel, which was comparable or better than Hayabusa/AMICA and strongly suggests that the images from the ONC-T could reconstruct the same accuracy of shape model as Itokawa.

Second, spectral sensitivity was quantitatively estimated for seven filter bands for the ONC-T using both Moon and Mars. The observation results indicate that the spectral response did not change since the pre-launch calibration using an integrating sphere. Comparison between disk-integrated lunar spectra with pre-launch calibration data and the spectral model based on Kaguya data suggests that ONC-T can reproduce spectrum of the Moon, one of the most accurately characterized spectral light source, suggests the possibility that the ONC-T can measure the spectra of the surface of asteroid Ryugu with high enough accuracy to examine the presence/absence and spatial distribution of spectroscopic features of hydrated minerals, such as 0.7 μm absorption band and UV absorption shoulder.

Third, the observations indicated that ONC-T suffered from considerably strong stray light, which was named “radiator stray light” under a certain range of spacecraft attitudes. However, the radiator stray light became negligibly weak outside this range. Because of the radiator stray lights, the stray light through the fore optics could not be examined with a very good detection limit. Nevertheless, the analysis of dark sky images with the moon outside the field of view indicated that the stray light from the fore optics was less than or equal to the level that could be quantified in a dark room prior to the launch.

In summary, the inflight calibration results indicates that the ONC of Hayabusa2 was in a good condition after the launch and strongly suggest that this camera system is capable of obtaining image data for scientific analysis necessary for the global and local characterization of Ryugu and selecting landing sites for sampling.

Acknowledgements.

The authors wish to thank two reviewers, Dr. S. Schröder and Dr. P. Lucey for their careful and constructive reviews, which greatly improved our manuscript. The authors also express their appreciations to Dr. S. Nakazawa, Dr. Y. Tsuda, Dr. S. Watanabe, Dr. K. Ogawa, and *Hayabusa2* team for supporting our calibration tests and inflight calibrations. The authors also wish to thank late Dr. Y. Iijima for supporting our activities. The research was supported by the Japan Society for the Promotion of Science (JSPS) KAKENHI (Grant Number 15J06330, 16H04059 and 17H01175) and Core-to-Core program "International Network of Planetary Sciences.”

References

ASTM committee (2006), 2000 ASTM Standard Extraterrestrial Spectrum Reference E-490-00 (http://rredc.nrel.gov/solar/spectra/am0/ASTM2000.html)

Benedetti, R., and Rossini, P. (1993). On the use of NDVI profiles as a tool for agricultural statistics: the case study of wheat yield estimate and forecast in Emilia Romagna. Remote Sensing of Environment, 45(3), 311-326

Binzel , R. P., A. W. Harris, S. J. Bus, and T. H. Burbine (2001), Spectral Properties of Near-Earth Objects: Palomar and IRTF Results for 48 Objects Including Spacecraft Targets (9969) Braille and (10302) 1989 ML, *Icarus*, *151*, 139-149.

Demura, H., S. Kobayashi, E. Nemoto, N. Matsumoto, M. Furuya, A. Yukishita, N. Muranaka, H. Morita, K. Shirakawa, M. Maruya, H. Ohyama, M. Uo, T. Kubota, T. Hashimoto, J. Kawaguchi, A. Fujiwara, J. Saito, S. Sasaki, H. Miyamoto, and N. Hirata (2006), Pole and Global Shape of 25143 Itokawa *, Science, 312*, 1347-1349.

Hatzianastassiou, N., Fotiadi, A., Matsoukas, C., Pavlakis, K., Drakakis, E., Hatzidimitriou, D., and Vardavas, I. (2004), Long-term global distribution of earth's shortwave radiation budget at the top of atmosphere. *Atmospheric Chemistry and Physics, 4(5)*, pp. 1217-1235.

Ishiguro, M., Nakamura, R., Tholen, D. J., et al. (2010), The Hayabusa Spacecraft Asteroid Multi-band Imaging Camera (AMICA), *Icarus*, *207*, 714- , doi:10.1016/j.icarus.2009.12.035

Ishiguro, M., Kuroda, D., Hasegawa, S., Kim, M. J., Choi, Y. J., Moskovitz, N., ... & Arai, A. (2014). Optical properties of (162173) 1999 JU3: in preparation for the JAXA Hayabusa 2 sample return mission. The Astrophysical Journal, 792(1), 74.

Kameda, S., H. Suzuki, T. Takamatsu, Y. Cho, T. Yasuda, M. Yamada, H. Sawada, R. Honda, T. Morota, C. Honda, M. Sato, K. Shibasaki, S. Ikezawa, S. Sugita (2017), Preflight calibration test results for optical navigation camera telescope (ONC-T) onboard the Hayabusa2 spacecraft, *Space Sci. Rev*., Vol 208, Issue 1–4, pp 17–31.

Kameda, S., H. Suzuki, Y. Cho, S. Koga, M. Yamada, T. Nakamura, T. Hiroi, H. Sawada, R. Honda, T. Morota, C. Honda, A. Takei, K. Takamatsu, Y. Okumura, M. Sato, T. Yasuda, K. Shibasaki, S. Ikezawa, S. Sugita (2015) Detectability of hydrous minerals using ONC-T camera onboard the Hayabusa-2 spacecraft. *Adv. Space Res. 56*, 1519-1524.

Kieffer, H. H (1997), Photometric Stability of the Lunar Surface. *Icarus, 130*, 323-327.

Kieffer, H.H. and T. C. Stone (2005), The spectral irradiance of the Moon, *Astron. J., 129*, 2887–2901.

Kouyama, T., Y. Yokota, Y. Ishihara, R. Nakamura, S. Yamamoto, T. Matsunaga (2016), Development of an Application Scheme for the SELENE/SP Lunar Reflectance Model for

Radiometric Calibration of Hyperspectral and Multispectral Sensors, *Planet. Space Sci., 124*, 76-83.

Lazzaro, D. M. A. Barucci, D. Perna, F. L. Jasmim, M. Yoshikawa, and J. M. F. Carvano (2013), Rotational spectra of (162173) 1999 JU3, the target of the Hayabusa2 mission, *Astron. Astrophys., 549*, L2.

Martonchik, J. V., Bruegge, C. J., and Strahler, A. H. (2000). A review of reflectance nomenclature used in remote sensing. Remote Sensing Reviews, 19(1-4), 9-20.

Matsuoka, M. and S. Kodama (2011), Coseismic displacement measurement of the 2010 El Mayor, Mexico earthquake by subpixel correlation from optical satellite images, *Proc. Geoscience and Remote Sensing Symposium (IGARSS), 2011 IEEE International*, 4010-4013.

Moskovitz, N. A., Abe, S., K. S. Pan, D. J. Osip, D. Pefkou, M. D. Melita, M. Elias, K. Kitazato, S. J. Bus, F. E. Demeo, R. O. Binzel, O. P. A. Abell (2013), Rotational characterization of Hayabusa II target Asteroid (162173) 1999 JU3, *Icarus, 224*, 24.

Ohtake, M., C. M. Pieters, P. Isaacson, S. Besse, Y. Yokota, T. Matsunaga, J. Boardman, S. Yamomoto, J. Haruyama, M. Staid, U. Mall, R. O. Green (2013), One Moon, Many Measurements 3: Spectral reflectance, *Icarus, 226*, 364-374.

Owen Jr, W. M. (2011). Methods of optical navigation. AAS Spaceflight Mechanics Conference. AAS 11-215.

Perna, D., Barucci, M. A., Ishiguro, M., Alvarez-Candal, A., Kuroda, D., Yoshikawa, M., ... & Müller, T. G. (2017). Spectral and rotational properties of near-Earth asteroid (162173) Ryugu, target of the Hayabusa2 sample return mission. Astronomy & Astrophysics, 599, L1.

Speyerer, E. J., R. Z. Povilaitis, M. S. Robinson, P. C. Thomas, R. V. Wagner (2016), Quantifying crater production and regolith overturn on the Moon with temporal imaging, *Nature, 538*, 215-218.

Sugita, S., T. Morota, S. Kameda, R. Honda, C. Honda, and Hayabusa-2 ONC Science Team, Science observations strategy for HAYABUSA-2 optical navigation cameras (ONC), *Lunar Planet. Sci. Conf., XXXXIII*, #3026, 2013a.

Sugita, S., D. Kuroda, S. Kameda, S. Hasegawa, S. Kamata, T. Hiroi, M. Abe, M. Ishiguro, N. Takato, M. Yoshikawa, Visible Spectroscopic Observations of Asteroid 162173 (1999 JU3) with the Gemini-S Telescope, *Lunar Planet. Sci. Conf., XXXXIII*, #2591, 2013b.

Tachibana, S. ,M. Abe, M. Arakawa, M. Fujimoto, Y. Iijima, M. Ishiguro, K. Kitazato, N. Kobayashi, N. Namiki, T. Okada, R. Okazaki, H. Sawada, S. Sugita, Y. Takano, S. Tanaka, S. Watanabe, M. Yoshikawa, H. Kuninaka and The HAYABUSA2 Project TEAM, Hayabusa2: Scientific importance of samples returned from C-type near-Earth asteroid (162173) 1999 JU3, *Geochemical Journal, 48*, 571, 2014.

Taylor, V., and Stowe, L. L.(1984), Reflectance characteristics of uniform Earth and cloud surfaces derived from NIMBUS-7 ERB. *Journal of Geophysical Research: Atmospheres*, 89(D4), 4987-4996.

Tsuda, Y., Yoshikawa, M., Abe, M., et al., System design of the Hayabusa 2—Asteroid sample return mission to 1999 JU3, *Acta Astronautica 91*, 356, 2013.

Yokota Y., T. Matsunaga, M. Ohtake, J. Haruyama, R. Nakamura, S. Yamamoto, Y. Ogawa, T. Morota, C. Honda, K. Saiki, K. Nagasawa, K. Kitazato, S. Sasaki, A. Iwasaki, H. Demura, N. Hirata, T. Hiroi, R. Honda, Y. Iijima, H. Mizutani (2011), Lunar photometric properties at wavelengths 0.5-1.6 μm acquired by SELENE Spectral Profiler and their dependency on local albedo and latitudinal zones, *Icarus, 215*, 639-660.

Vilas, F., Spectral characteristics of Hayabusa 2 Near-Earth Asteroid targets 162173 1999 JU3 and 2001 QC34, *Astron. J., 135*, 1101, 2008

Wyszecki, G., and Stiles, W. S. (1982). Color science (second edition). New York: Wiley.